Title:

Supplementary Materials for " Superionic Behavior and Defect Robustness in $LiNbOCl_4$: A First-Principles Molecular Dynamics Study"

Authors

Halimah Harfah[1], Yoshitaka Tateyama[1,2], Kazunori Takada[1] and Randy Jalem[1,*]

[1]Research Center for Energy and Environmental Materials (GREEN), National Institute for Materials Science (NIMS), 1-1 Namiki, Tsukuba, Ibaraki 305-0044, Japan

[2]Laboratory for Chemistry and Life Science, Institute of Integrated Research, Institute of Science Tokyo, 4259 Nagatsuta-cho, Midori-ku, Yokohama, Kanagawa 226-8501, Japan

*Email: JALEM.Randy@nims.go.jp

Abstract:

This supplementary materials provides detailed computational data and analyses supporting the main text of the study "Superionic Behavior and Defect Robustness in $LiNbOCl_4$: A First-Principles Molecular Dynamics Study." We first present a high-throughput screening of 1,000 randomly generated lithium configurations using Ewald summation to identify electrostatically favorable arrangements. The correlation between Ewald energy and minimum Li–Li distance is discussed to elucidate repulsion effects. Next, we evaluate the formation energy of Schottky defects, revealing the moderate energetic cost of generating Li and Cl vacancies under equilibrium conditions. Phase stability of both pristine and defected $LiNbOCl_4$ is examined through convex hull construction, indicating marginal metastability with energy values slightly above the hull. Finally, we detail density functional theory and molecular dynamics (AIMD) simulation parameters, including Langevin thermostat settings and the evolution of system properties such as temperature, volume, and lattice angles across a range of thermal conditions. These results collectively support the structural and dynamical robustness of $LiNbOCl_4$ under superionic operating conditions.

S1. Ewald and Total Energy Screening for Lithium Configurations

The initial structural model for $LiNbOCl_4$ is based on experimental crystallographic data reported for the tetragonal phase (space group I4/m)[1]. The lattice parameters are set to $a = b = 8.9109$ Å and $c = 3.9542$Å, with angles $\alpha = \beta = \gamma = 90°$. The atomic site coordinates and occupancies are summarized in Table S1

Table S1. Crystallographic Parameters, Atomic Site Occupancies, and Structural Coordinates for $LiNbOCl_4$ (Space Group I 4/m)[2]. This table summarizes the lattice parameters and atomic positions within the $LiNbOCl_4$ structure, specifying atomic coordinates and partial occupancies for Li sites based on crystallographic symmetry and experimental disorder.

Lattice parameters (space group I 4/m)					
a	b	c	α	β	γ
8.91090	8.91090	3.95420	90°	90°	90°

Atom	x	y	z	Site	Occupancy
Nb	0.00000	0.00000	0.00000	2a	1.000
O	0.00000	0.00000	0.50000	2b	1.000
Cl	0.07270	0.25000	0.00000	8h	1.000
Li(1)	0.07100	0.51800	0.00000	8h	0.040
Li(2)	0.39600	0.69700	0.00000	8h	0.170

Li(3)	0.16700	0.68800	0.00000	8h	0.040

To assess the electrostatic stability of $LiNbOCl_4$ across various lithium configurations, Ewald energy calculations were performed on 1,000 randomly generated structures by using pymatgen libraries[3]. Figure S1(a) presents the distribution of Ewald energies, with the configurations ordered by ascending energy. The lowest-energy structures, highlighted in the inset, reveal that specific lithium arrangements result in more electrostatically favorable configurations. Figure S1(b) correlates Ewald energy with the minimum Li–Li distance, demonstrating that configurations with short Li–Li separations (<1.5 Å) correspond to higher Ewald energies due to increased Coulombic repulsion. In contrast, larger Li–Li separations (>2.5 Å) are associated with lower energies, indicating more favorable electrostatic environments. This screening strategy enables efficient pre-selection of low-energy configurations for subsequent first-principles calculations.

(a)

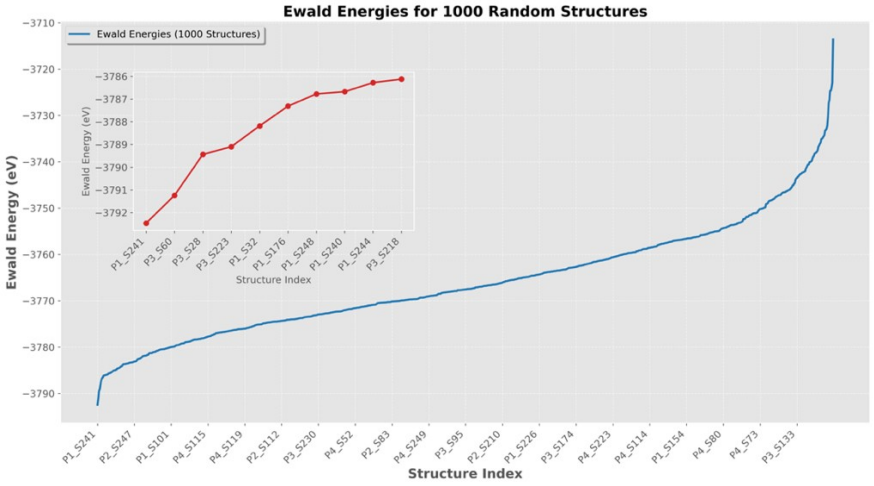

(b)

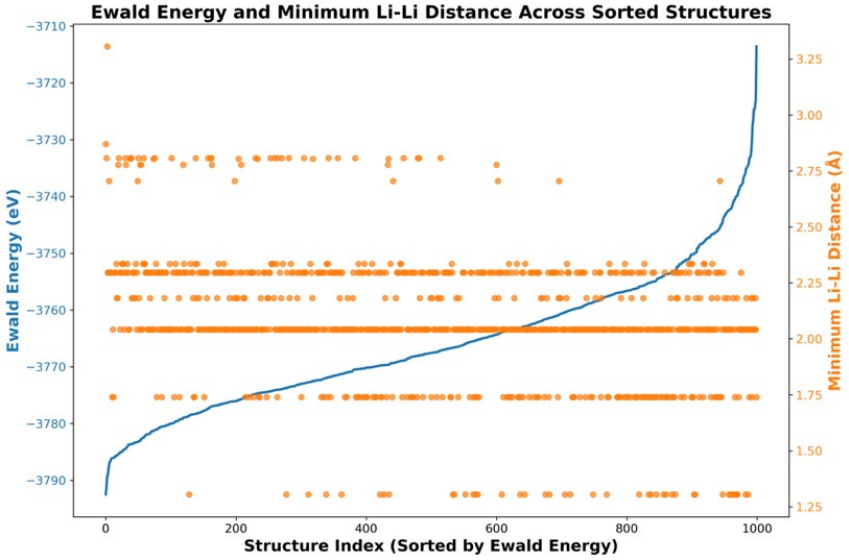

Figure S1. Distribution of Ewald Energies for 1,000 Randomly Generated $LiNbOCl_4$ Configurations. (a) The plot illustrates the distribution of Ewald energies across 1,000 randomly generated structures of $LiNbOCl_4$, ordered by ascending energy. The main curve (solid blue line) represents the Ewald energy (in eV) for each structure, capturing variations in electrostatic energy resulting from different lithium arrangements. The inset (solid red line curve) highlights the lowest energy configurations, with notable structures labeled (e.g., P1_S241, P3_S60), providing a detailed view of the configurations achieving minimal Ewald energy. This

analysis reveals that specific lithium site occupancies significantly influence electrostatic favorability within the system. (b) Ewald Energy and Minimum Lithium-Lithium Distance Across Sorted Structures. The graph depicts the Ewald energy (blue line) and minimum lithium-lithium (Li-Li) distance (orange scatter points) for 1000 structures sorted by ascending Ewald energy. The left y-axis represents the Ewald energy (eV), while the right y-axis corresponds to the minimum Li-Li distance (Å). The blue line indicates the electrostatic contribution to the lattice energy, while the orange scatter points capture the shortest Li-Li distances within each structure. Shorter Li-Li distances (<1.5 Å, orange) dominate higher Ewald energy regions, reflecting less favorable electrostatic configurations due to increased repulsion. In contrast, longer Li-Li distances (>2.5 Å) are more prevalent in the lower Ewald energy range, corresponding to more favorable electrostatic configurations with reduced repulsion. The color assignments distinguish the trends in Ewald energy and minimum Li-Li distances, highlighting their interplay across the sorted structures.

LiNbOCl4 with LiCl Schottky defects

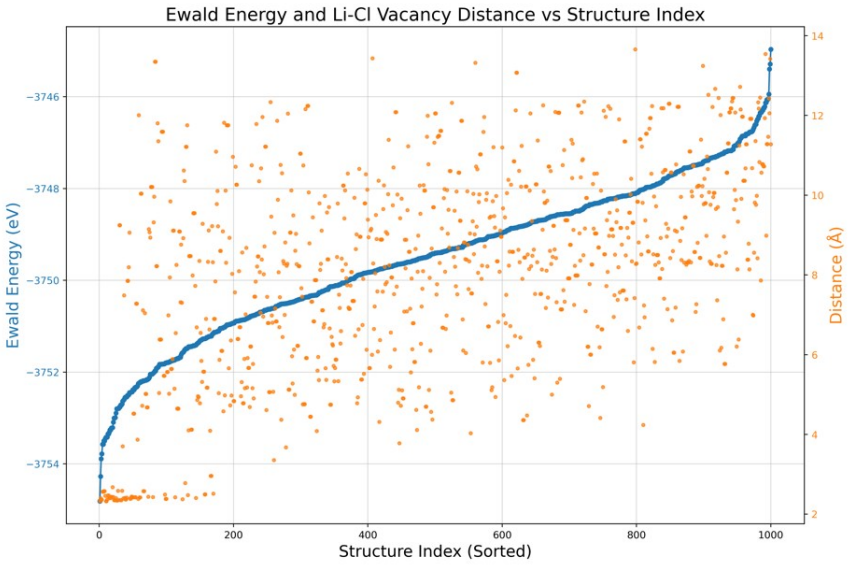

Figure S1-2. Correlation Between Ewald Energy and Li-Cl Vacancy Distance in $LiNbOCl_4$ with LiCl Schottky Defects. This graph illustrates the relationship between Ewald energy (blue line) and Li-Cl vacancy distance (orange scatter points) in 1000 configurations of $LiNbOCl_4$ with LiCl Schottky defects, sorted by structure index. The Ewald energy (left vertical axis) is represented by a blue curve, showing a monotonic increase from approximately −3754 eV to −3746 eV as the structure index increases. Lower Ewald energies correspond to more favorable electrostatic configurations. The Li-Cl vacancy distance (right vertical axis) is depicted as orange scatter points, ranging from 2 Å to 14 Å. Compact vacancy distances (<4 Å) dominate at lower structure indices and correlate with lower Ewald energies, suggesting efficient charge interactions. In contrast, extended distances (>10 Å) are more prevalent at higher structure indices and are associated with higher Ewald energies, reflecting less favorable electrostatic configurations.

The graph (fig. S1-2) provides a detailed analysis of the relationship between Ewald energy and Li-Cl vacancy distance in $LiNbOCl_4$ containing LiCl Schottky defects. The Ewald energy, which reflects the electrostatic component of the system's total energy, is plotted against the sorted structure index (blue curve) to highlight variations in electrostatic configurations among different defect structures. Simultaneously, the orange scatter points represent the Li-Cl vacancy distances, offering insight into how defect geometry influences electrostatic interactions in the lattice.

The Ewald energy shows a steady increase with the structure index, starting around −3754 eV and reaching approximately −3746 eV. This trend indicates that configurations with lower indices are more electrostatically favorable due to optimized charge interactions. These lower-energy configurations suggest defect geometries where the Li-Cl vacancies are positioned to minimize repulsive interactions and maximize the electrostatic balance in the lattice. In contrast, higher-energy configurations (larger structure indices) likely result from less

favorable arrangements, such as larger separations between defects or irregular distributions, which lead to increased Coulombic repulsion.

The Li-Cl vacancy distances, represented by the orange scatter points, span a broad range from approximately 2 Å to 14 Å. Configurations at lower structure indices, corresponding to lower Ewald energies, are predominantly associated with shorter vacancy distances (<4 Å). These compact defect geometries facilitate strong electrostatic interactions between the lithium and chlorine vacancies, which help maintain the overall electrostatic balance within the system.

As the structure index increases, the vacancy distances become more dispersed, with a noticeable increase in configurations exhibiting longer vacancy distances (>10 Å). These extended defect separations lead to less favorable electrostatic configurations due to weakened interactions between the vacancies and an increase in long-range Coulombic repulsion. This dispersion highlights the diversity of defect arrangements and their direct influence on the Ewald energy.

The correlation between shorter Li-Cl vacancy distances and lower Ewald energies underscores the significant influence of defect geometry on electrostatic interactions. Compact defect pairs lead to stronger interactions and reduced total electrostatic energy, aligning with principles of charge distribution in ionic systems. Conversely, configurations with dispersed vacancies exhibit higher Ewald energies, reflecting less efficient charge arrangements. The gradual increase in both energy and vacancy distances with the structure index suggests a broad sampling of defect configurations, from highly optimized to less favorable geometries.

The observed trends provide valuable insights into the role of Li-Cl Schottky defects in shaping the electrostatic landscape of $LiNbOCl_4$. Configurations with shorter Li-Cl distances are energetically favorable and may offer pathways for improved ion transport by reducing electrostatic barriers. On the other hand, configurations with longer vacancy distances, though less favorable in terms of Ewald energy, may represent structural variations that could influence other material properties, such as ion diffusion or defect dynamics. These results highlight the critical role of defect geometry in determining the electrostatic characteristics of the material, which are closely tied to its performance in solid-state battery applications.

S2. Defect Formation Energy

S2-1. Defect formation energies from a $LiCl/NbCl_3O$-referenced phase diagram

All defect energetics were evaluated in a 2×2×3 $LiNbOCl_4$ supercell (24 f.u., 168 atoms) using the same DFT settings as in the main text. To place Schottky, Frenkel, and antisite defects on a common thermodynamic footing, we adopted chemical potentials consistent with the $LiNbOCl_4 \leftrightarrow NbCl_3O + LiCl$ equilibrium.

We denote the elemental chemical potentials as μ_{Li}, μ_{Nb}, μ_O, and μ_{Cl}. For $LiNbOCl_4$, LiCl, and $NbCl_3O$ we have the relations

$$\mu_{Li} + \mu_{Nb} + \mu_O + 4\mu_{Cl} = E_{tot}(LiNbOCl_4),$$
$$\mu_{Li} + \mu_{Cl} = E_{tot}(LiCl), \quad \mu_{Nb} + 3\mu_{Cl} + \mu_O = E_{tot}(NbCl_3O),$$

so that the $LiNbOCl_4$ chemical potentials are fixed by coexistence with LiCl and $NbCl_3O$. In practice, the LiCl chemical potential is taken from a separate bulk LiCl calculation ($Fm\bar{3}m$, 4 f.u., $E_{tot}(LiCl, 4\text{ f.u.}) = -30.004565$), giving

$$\mu_{LiCl} \equiv \mu_{Li} + \mu_{Cl} = \frac{E_{tot}(LiCl, 4 \text{ f.u.})}{4} \approx -7.50\ f.u..$$

S2-2 LiCl Schottky pair ($V_{Li} + V_{Cl}$)

A LiCl Schottky pair is introduced by removing one Li and one Cl atom from the 2×2×3 $LiNbOCl_4$ supercell, corresponding to one LiCl unit per 24 formula units. The DFT total energies of the pristine and Schottky-defected supercells are

$$E_{pristine} = -863.190880\ eV$$

$$E_{schottky} = -856.667858\ eV$$

so that

$$\Delta E = E_{Schottky} - E_{pristine} = 6.523022\ eV$$

Using the standard defect formation expression

$$E_f = E_{defect} - E_{pristine} - \sum_i n_i \mu_i,$$

with $n_{Li} = n_{Cl} = -1$ for the Schottky pair and $\mu_{Li} + \mu_{Cl} = \mu_{LiCl}$, the LiCl-Schottky formation energy becomes

$$E_f^{Sch} = E_{Schottky} - E_{pristine} + \mu_{LiCl} = \Delta E + \mu_{LiCl} \approx 6.523022 - 7.5011 \approx -0.98\ eV$$

Thus, within the LiCl/$NbCl_3O$-referenced chemical potential scheme, the LiCl-deficient composition is thermodynamically favored relative to pristine $LiNbOCl_4$, consistent with the convex-hull analysis where the Schottky composition lies slightly closer to the $NbCl_3O$ + LiCl tie-line ($\Delta E_{hull} \approx 0.0185$ vs 0.0211 eV atom^{-1}).

S2-3 Li Frenkel and antisite pairs

Li Frenkel ($V_{Li} + Li_i$) and antisite (O↔Cl and Li↔Nb) defects preserve the overall $LiNbOCl_4$ stoichiometry. For such stoichiometric defects, the chemical potential terms cancel, and the formation energy reduces to the total-energy difference

$$E_f^{stoich} = E_{defect} - E_{pristine}.$$

Instead of tabulating all absolute total energies, we extract these differences from the **decomposition energies** (convex-hull distances) computed with Pymatgen using the same DFT database. For the pristine $LiNbOCl_4$ cell we obtain $E_{hull}^{pris} \approx 0.0211$ eV/atom. The Frenkel supercell (one $V_{Li} + Li_i$ pair in 168 atoms) relaxes to $E_{hull}^{Frenkel} \approx 0.0245\ eV/atom$ giving a per-atom increase

$$\Delta e_{Frenkel} = E_{hull}^{Frenkel} - E_{hull}^{pris} \approx 0.0034 \text{ eV/atom}$$

Multiplying by the number of atoms (N = 168) yields the approximate Frenkel pair formation energy:

$E_f^{Frenkel\ pair} \approx N\,\Delta e_{Frenkel} \approx 0.0034 \times 168 \approx 0.6$ eV

Similarly, O↔Cl and Li↔Nb antisite supercells exhibit $E_{hull}^{antisite} \approx 0.030–0.033$ eV/atom. Relative to the pristine hull distance this corresponds to

$\Delta E_{antisite} \approx 0.0089–0.0119$ eV/atom

and hence

$E_f^{antisite\ pair} \approx N\,\Delta e_{antisite} \approx 1.5–2.0$ eV per pair

These hull-based estimates share the same LiCl/$NbCl_3O$-referenced μ-environment as the Schottky LiCl-reservoir picture and are therefore directly comparable. While the absolute energies carry the usual DFT and phase-diagram uncertainties (on the order of a few 0.1 eV), the relative ordering is robust: within this framework the LiCl Schottky configuration is thermodynamically preferred, the Li Frenkel pair is moderately penalized, and antisite defects are strongly disfavored.

S2.4 Summary of defect energetics

Table S2.4 summarizes the defect formation energies (per defect pair) obtained from the LiCl/$NbCl_3O$-referenced phase-diagram analysis.

Table S2.4 the defect formation energies (per defect pair) obtained from the LiCl/$NbCl_3O$-referenced phase-diagram analysis

Defect type	**Supercell composition**	ΔE_{hull} **(eV/atom)**	E_f **(eV per pair)**
Pristine	$Li_{24}Nb_{24}Cl_{96}O_{24}$	0.0211	–
LiCl Schottky (V_{Li} + V_{Cl})	$Li_{23}Nb_{24}Cl_{95}O24$	0.0185	≈ –1.0
Li Frenkel (V_{Li} + Li_i)	$Li_{23}Nb_{24}Cl_{95}O24$ (stoichiometric)	0.0245	≈ 0.6
O↔Cl / Li↔Nb antisite pair	$Li_{23}Nb_{24}Cl_{95}O24$ (stoichiometric)	0.030–0.033	≈ 1.5–2.0

Within the LiCl/$NbCl_3O$-consistent chemical potential scheme, LiCl-Schottky disorder is thus the thermodynamically least penalized defect motif, Li Frenkel pairs are moderately costly, and antisite defects are significantly more unfavorable. This hierarchy motivates our focus on LiCl-Schottky disorder in the AIMD analysis of Li-ion transport.

S3. Convex Hull Analysis and Decomposition Energy Evaluation

To rigorously evaluate the thermodynamic stability of the pristine and Schottky-defected $LiNbOCl_4$ structures, we adopted the convex hull construction methodology as detailed in the previous paper[4]. This approach involves calculating the decomposition energy (E_d) of a given phase relative to the most stable phase assemblage at that composition.

At normal pressure and T=0 K, the Gibbs free energy simplifies to the total internal energy (E):

$G(T = 0,P,N_i) = E(T = 0,P,N_i)$

Here, N_i is the number of atoms of element i, and E is the total energy computed from DFT calculations.

The normalized formation energy at composition (x_{Li}, x_{Nb}, x_{Cl}, x_O) is:

$$E_{form}(x_i) = \frac{E_{phase} - \sum_i N_i \mu_i}{\sum_i N_i \mu_i}$$

Where μ_i are the chemical potentials of the elemental reference states. In this work, elemental lithium (Li), niobium (Nb), chlorine (Cl_2 gas), and oxygen (O_2 gas) were used as references.

The convex hull is constructed by identifying all the phases whose formation energies lie on the lowest-energy envelope in the multicomponent composition space. Mathematically, for any phase, its decomposition energy above the convex hull is expressed as:

$$E_d = E_{phase} - E_{hull}$$

Where E_{phase} is the formation energy of the phase under study, E_{hull} is the interpolated energy of the convex hull surface at the same composition. Phases with $E_d = 0$ lie on the convex hull and are considered thermodynamically stable at 0 K. Phases with $E_d > 0$ are metastable and may decompose into adjacent ground-state phases. This methodology can rigorously determine the proximity of the calculated structures to the thermodynamic stability limit, thereby providing a physically sound metric for assessing their synthesizability. In this study, E_d values were computed using phase diagram analysis implemented in the Pymatgen library[3], with thermodynamic reference data obtained from the Materials Project database[5]. This combined formalism enables systematic and reproducible evaluation of phase stability across multicomponent systems

As shown in Figure S3, both pristine and defected $LiNbOCl_4$ structures lie slightly above the convex hull, with formation energies of 0.021 eV/atom and 0.018 eV/atom, respectively. While these values indicate marginal thermodynamic instability, they fall within the metastability range commonly observed for experimentally synthesizable compounds. Notably, some defected structures exhibit lower energy above-hull values than the pristine phase, suggesting that local lattice relaxation or favorable bonding environments may compensate for the energy cost of defect formation. These results emphasize the importance of considering both thermodynamic and kinetic factors when evaluating phase stability.

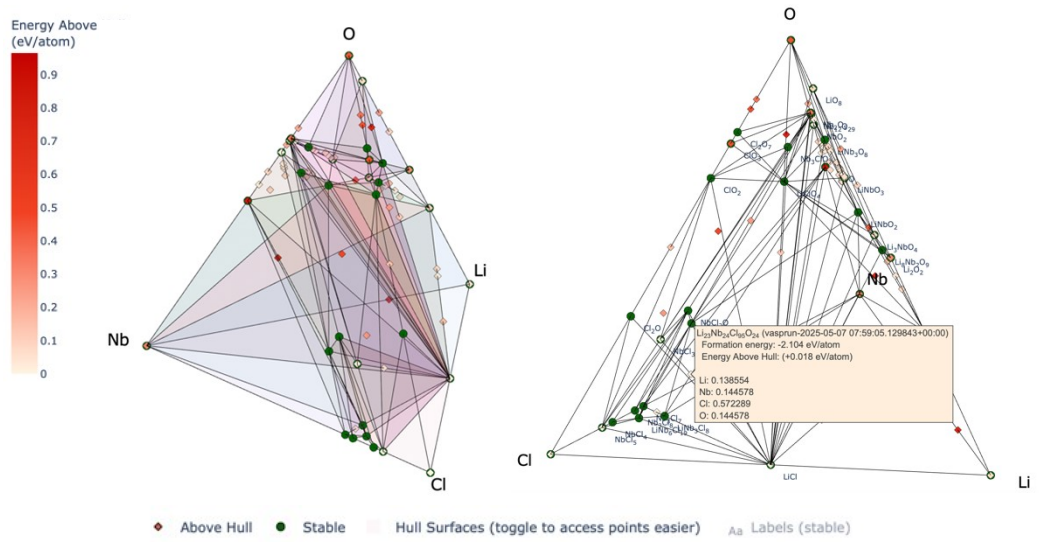

Figure S3. Phase Stability Diagram for the Li–Nb–Cl–O System, pristine (left) and Schottky-defected $LiNbOCl_4$ (right). This ternary phase stability diagram for the Li–Nb–Cl–O system depicts the formation energy of various compounds, with $LiNbOCl_4$ shown as a slightly unstable phase, with 0.021 eV/atom (pristine) and 0.018 eV/atom (Schottky) energy above the convex hull. Each vertex represents a pure element (Li, Nb, Cl, O), and the green points within the tetrahedron represent stable compounds with their respective compositions and formation energies. The highlighted point for $LiNbOCl_4$, with a formation energy of -2.10 eV/atom. Despite the positive defect formation energy, some defected configurations show lower energy above hull values than pristine structures, likely due to favorable lattice relaxation or local bonding environments, highlighting the need to consider both thermodynamic and kinetic factors

S4. Density Functional Theory and Molecular Dynamics Simulation Parameters

Density functional theory and molecular dynamics (AIMD) simulations were performed to explore the thermal and dynamic behavior of $LiNbOCl_4$ at elevated temperatures. Simulations were conducted using a Langevin thermostat with damping constants γ = 10 and 100, across target temperatures ranging from 600 K to 1400 K. The total simulation time spans 20,000 steps, focusing on the initial equilibration phase. Figures S4-1 to S4-4 demonstrate stabilization of F and E_0 ($\sigma \rightarrow 0$, where σ (in eV) is the smearing width controlling the broadening of orbital occupancies around the Fermi level) and temperature over simulation time, indicating effective thermal equilibration. The average temperatures achieved for each γ value are summarized in Table S4, showing close agreement with target temperatures, especially for γ = 10. Figures S4-5 and S4-6 show that lattice angles remain stable throughout the simulation, while Figures S4-7 and S4-8 illustrate thermal expansion via volume fluctuations at higher temperatures. These simulations confirm structural robustness and provide a reliable basis for investigating superionic behavior in $LiNbOCl_4$ under operational conditions.

Using the equilibrium volumes obtained from NPT simulations, additional DFT–MD runs were performed under NVT conditions, as discussed in the main text. Figures S4-9 and S4-13 report the evolution of the free energy (F) and the zero-entropy energy (E_0) during the NVT trajectories. Across all temperatures, both quantities remain bounded and fluctuate around a stable mean after the initial transient, confirming numerical stability and adequate thermalization of the trajectories. As expected, the fluctuation amplitude increases with temperature due to enhanced anharmonic lattice motion. No abrupt discontinuities are observed in F or E_0, consistent with the absence of structural instability over the simulated time window.

For the Schottky-defected system, the corresponding NPT and NVT trajectories (Figures S4-10 to S4-13) show similarly stable behavior: after rapid equilibration to the target temperature, F and E_0 display only thermally

induced fluctuations without signatures of runaway behavior. These results validate the robustness of the sampling protocol used for the subsequent transport analyses (MSD, van Hove functions, and ionic conductivity) reported in the main text.

The temperature evolution shown in Figure S4-11 demonstrates that the Schottky-defected $LiNbOCl_4$ system rapidly equilibrates within the first ~1,000 steps across all target temperatures. The temperature fluctuations thereafter remain within a narrow range, consistent with expected thermal noise, confirming effective thermostat performance and reliable thermalization throughout the simulation window. These observations validate the robustness of the thermodynamic sampling used for subsequent analyses. Complementary behavior is observed in the volume evolution plots shown in Figure S4-12. Following initial thermal expansion, each system exhibits volume fluctuations characteristic of thermal motion and pressure relaxation. Notably, the amplitude of these fluctuations increases with temperature, particularly at 1400 K, indicating stronger anharmonic lattice dynamics and thermal expansion. This behavior supports the onset of dynamic ionic activity, an essential feature of superionic conductors, and reinforces the conclusion that the system remains structurally stable yet dynamically active under elevated thermal conditions.

In the main text (Fig. 3), we report the species-averaged Einstein mean-square displacement, $\langle|r_i(t+\Delta t)-r_i(t)|^2\rangle$, evaluated from periodic-image–unwrapped trajectories with multi time-origin averaging and center-of-mass (COM) drift correction using pymatgen's Diffusion Analyzer.[6,7] Under periodic boundary conditions, Li ions can traverse multiple unit cells over long Δt; therefore, the MSD is not bounded by the simulation box length squared L^2 and grows linearly in the diffusive regime ($\langle\Delta r^2\rangle \approx 6D$t in 3D). Accordingly, MSD values on the order of 1500 $Å^2$ correspond to an RMS displacement $\sqrt{MSD} \approx 39$ Å, which is physically reasonable for several cell crossings given our cell dimension of ~16 Å. To exclude analysis artefacts, we independently recomputed the Li MSD using a custom Python workflow that explicitly implements trajectory unwrapping and Li-only COM subtraction; the resulting COM-corrected MSD agrees with the DiffusionAnalyzer curve within ~5–10% over the full 100-ps window, and the difference between corrected and uncorrected MSD remains below 10% of the final value. In addition, the RMS value previously quoted (~27 Å) corresponds to a time-averaged RMS displacement over the entire 0–100 ps window, $r_{RMS} = \langle\sqrt{MSD(\Delta t)}\rangle_{\Delta t}$, rather than √(MSD at 100 ps). Because this average weights early (small-displacement) and late (large-displacement) times together, r_{RMS} is expected to be lower than the terminal RMS at 100 ps, explaining the difference between ~27 Å and ~39 Å.

We also note that the diffusion coefficient extracted from the COM-corrected MSD at 1000 K, $D \approx 1.5\times10^{-4}$ cm^2 s^{-1}, lies within the range commonly reported by AIMD studies of Li superionic conductors at comparable temperatures (10^{-5}–10^{-3} cm^2 s^{-1}).[6–8] This consistency, together with the stable thermodynamic trajectories described above, supports that the transport properties obtained here are physically meaningful and that the derived room-temperature conductivities and activation energies are in good agreement with available experimental data for $LiNbOCl_4$.[1,2,9]

Similar to the pristine system, AIMD simulations under NVT conditions were performed for the Schottky-defected $LiNbOCl_4$ using volumes obtained from prior NPT simulations, as discussed in the main text. Figure S4-13 presents the evolution of F, and E_0 during simulations with a Langevin thermostat at fixed volume. The close alignment between F and E_0 across all temperatures confirms F and E_0 ($\sigma\rightarrow0$) remain bounded and fluctuate around stable means after the initial transient, confirming numerical stability and adequate thermalization.

Overall, the AIMD simulations conducted under both NPT and NVT conditions provide comprehensive insights into the thermal response and structural stability of pristine and Schottky-defected $LiNbOCl_4$ across a broad

temperature range (600–1400 K). The consistent stabilization of energy, temperature, volume, and pressure-related components confirms effective thermal equilibration and robust lattice behavior under varying thermodynamic ensembles. Notably, the enhanced fluctuations observed at elevated temperatures, particularly in volume and pressure, indicate increased anharmonic lattice activity and the onset of dynamic ionic motion, a hallmark of superionic behavior. The absence of structural collapse or mechanical instability in both pristine and defected systems further highlights the material's intrinsic defect tolerance.

These results affirm the reliability of the AIMD simulations and provide a solid foundation for subsequent analyses. Therefore, the investigations of mean squared displacement (MSD), ion trajectories, and ionic conductivity discussed in the main text can be considered credible and physically meaningful. Together, these findings demonstrate that $LiNbOCl_4$ is both thermally stable and dynamically active under high-temperature conditions, supporting its potential as a superionic conductor in solid-state energy devices.

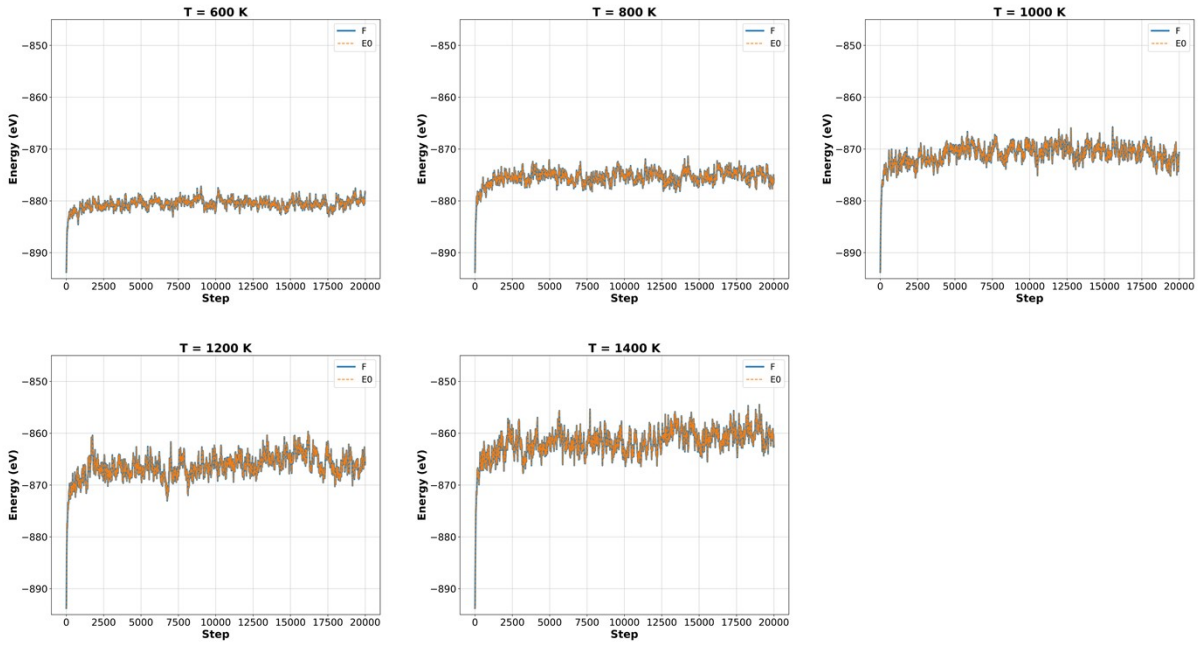

Figure S4-1 Energy profiles (F and E_0) of pristine $LiNbOCl_4$ system across simulation steps at 600–1400 K using a Langevin thermostat with Langevin Gamma = 100. Energy stabilization is achieved with minor fluctuations indicative of thermal activity.

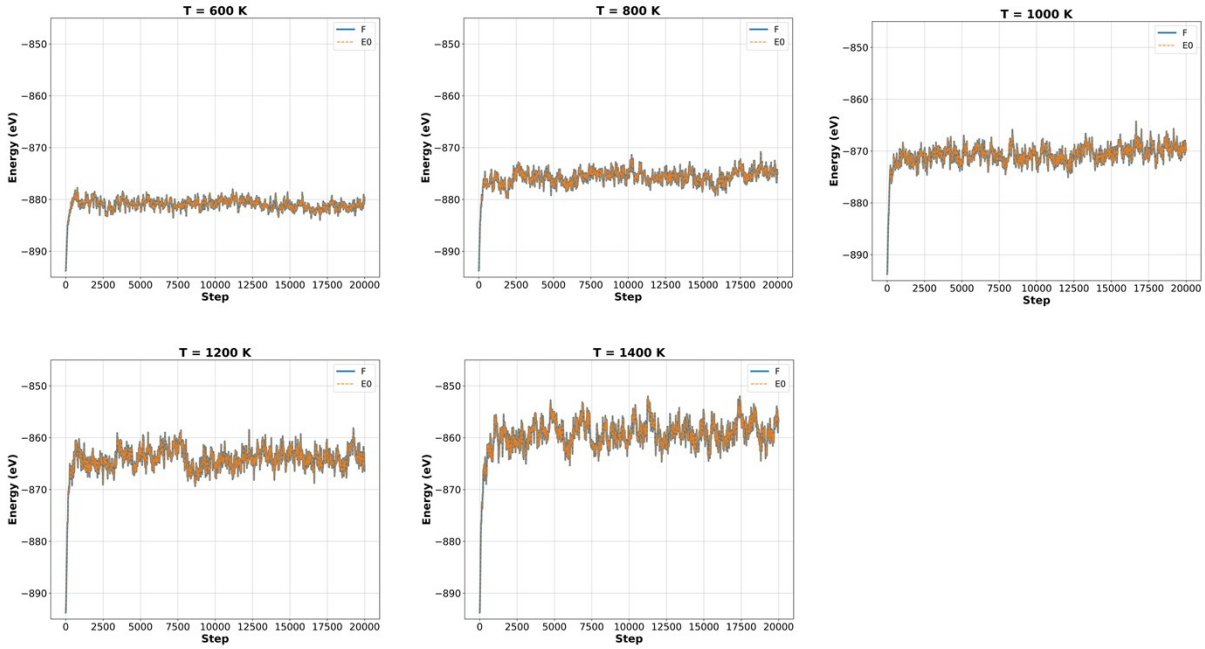

Figure S4-2 Energy profiles (F and E_0) pristine $LiNbOCl_4$ system across simulation steps at 600–1400 K using a Langevin thermostat with Langevin gamma = 10. Energy stabilization occurs after the equilibration phase.

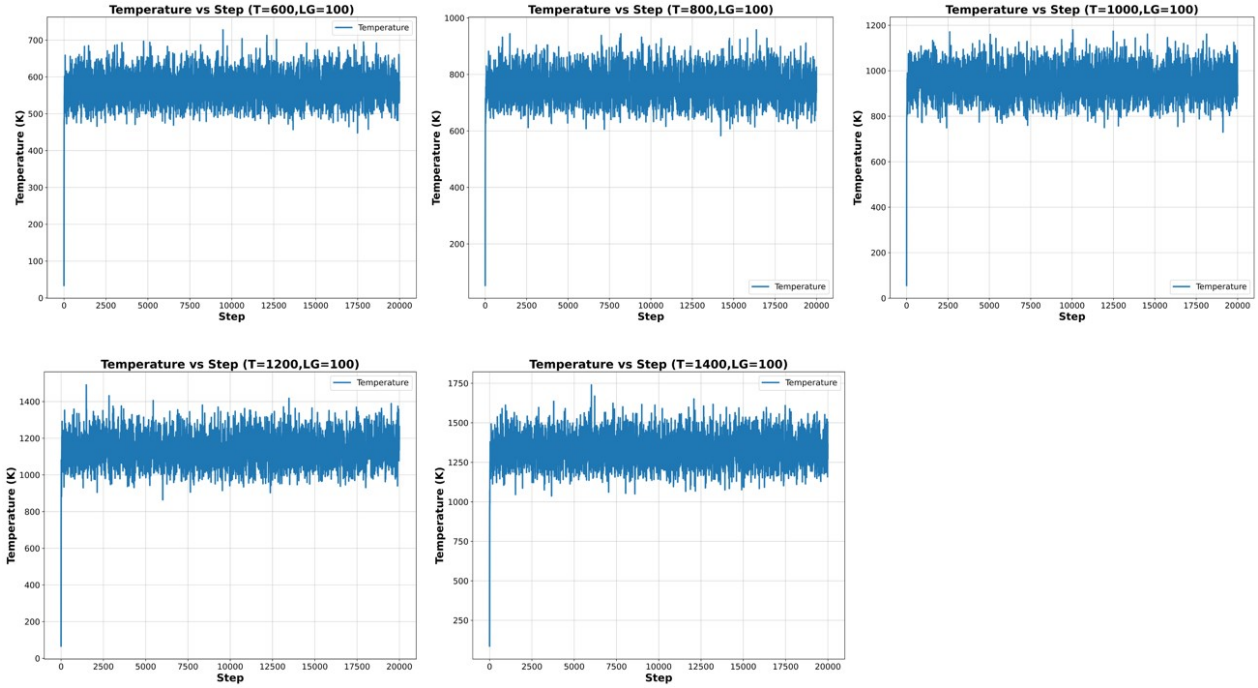

Figure S4-3 Temperature profiles of pristine $LiNbOCl_4$ system for Langevin gamma = 100 across target temperatures (600–1400 K). Despite rapid equilibration, average temperatures deviate slightly from set points.

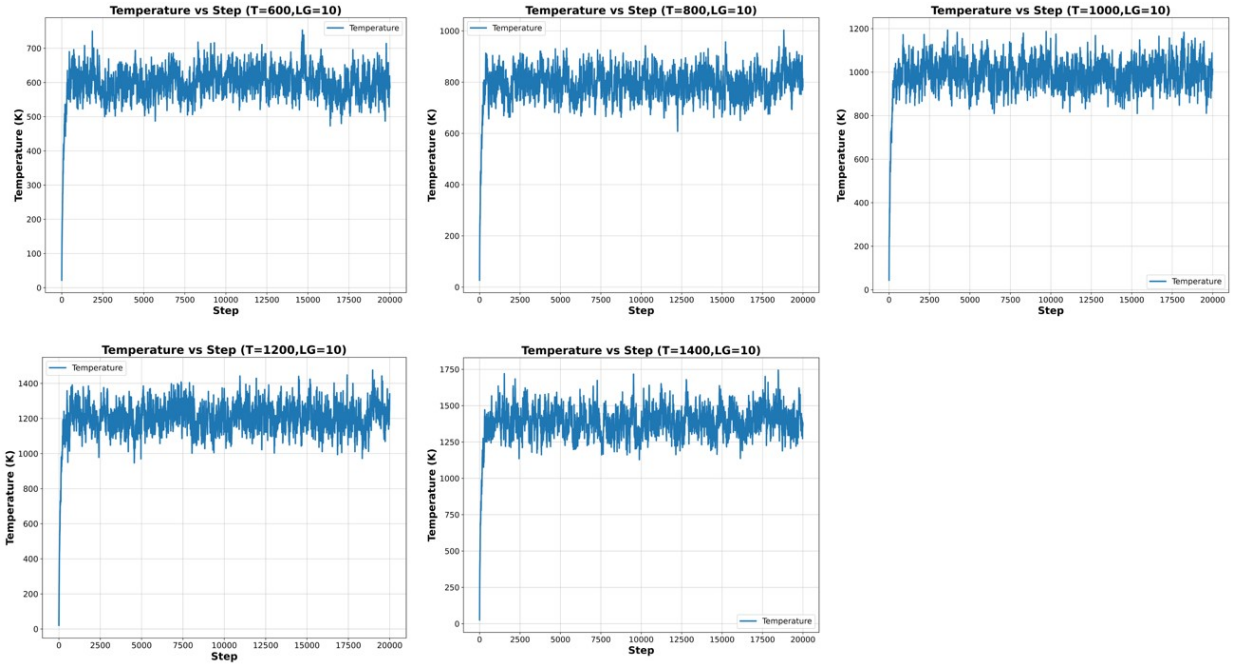

Figure S4-4 Temperature profiles of pristine $LiNbOCl_4$ system for Langevin gamma = 10 across target temperatures (600–1400 K). The average temperatures closely match set points, particularly at higher temperatures.

Table S4-1. Average Temperature Comparison

Temperature (K)	Average Temperature for Different Langevin_Gamma	
	100	10
600	570.81	601.35
800	761.63	796.91
1000	951.33	987.16
1200	1141.13	1210.20
1400	1130.26	1401.06

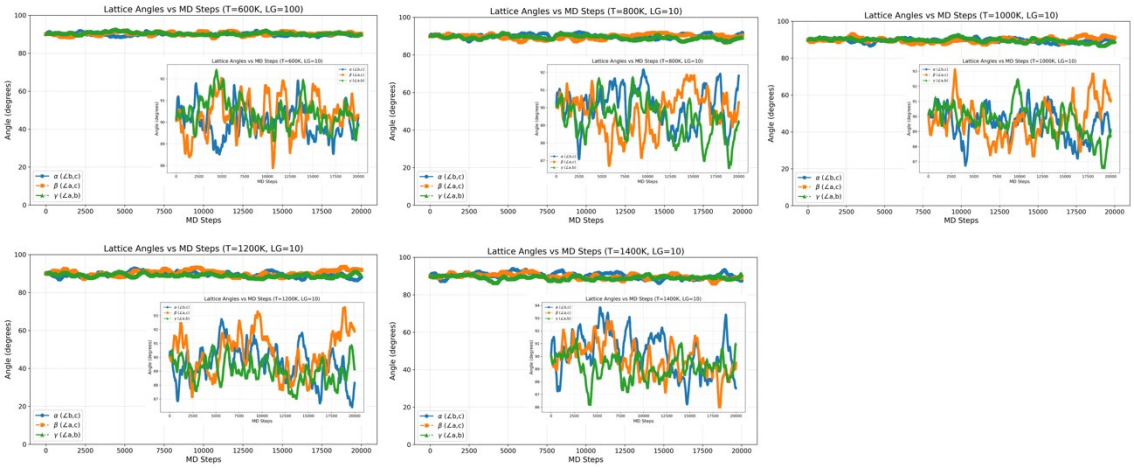

Figure S4-5. Evolution of lattice angles (α, β, γ) of pristine $LiNbOCl_4$ system across simulation steps at temperature of 600–1400 K for Langevin gamma = 100. Angles remain stable despite minor thermal-induced fluctuations. The blue line represents α (∠b,c), the orange line represents β (∠a,c), and the green line represents γ (∠a,b).

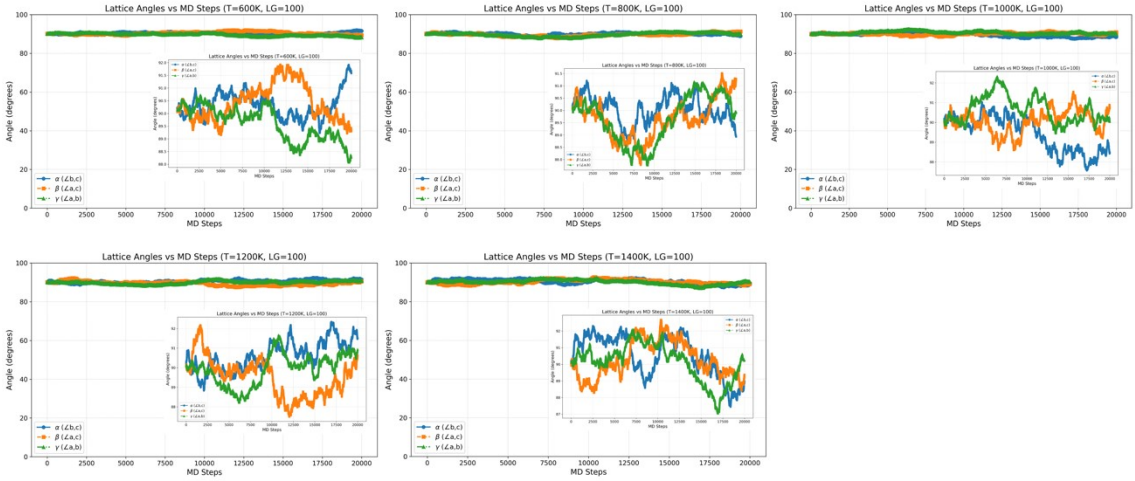

Figure S4-6 Evolution of lattice angles (α, β, γ) of pristine $LiNbOCl_4$ system across simulation steps at temperatures of 600–1400 K for Langevin gamma = 10. Angles exhibit stable behavior throughout the simulation. The blue line represents α (∠b,c), the orange line represents β (∠a,c), and the green line represents γ (∠a,b).

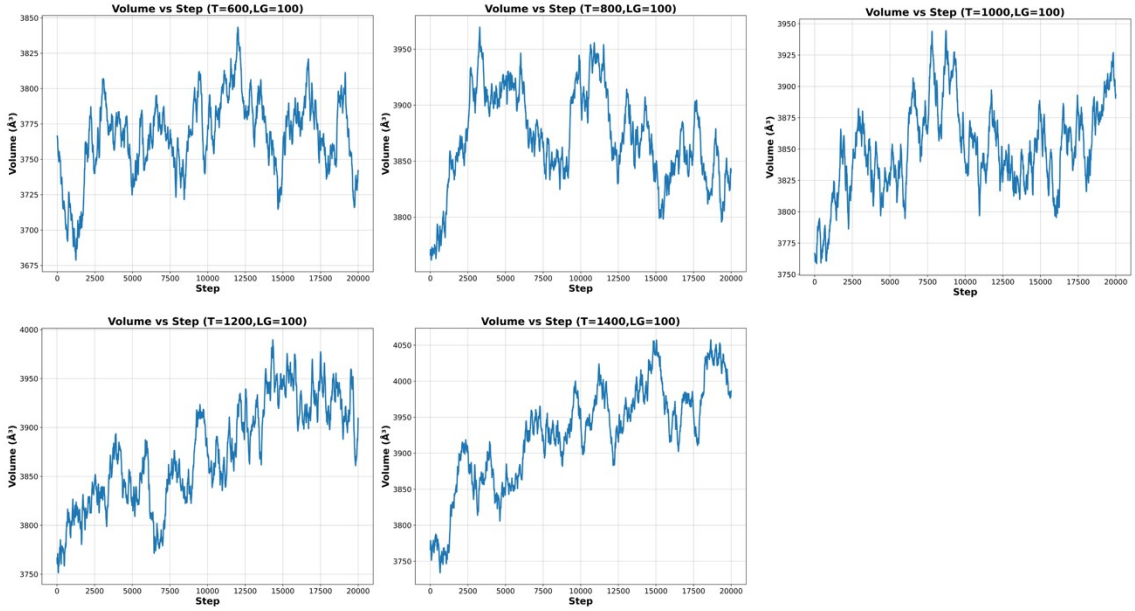

Figure S4-7 Volume fluctuations of pristine $LiNbOCl_4$ system across simulation steps at temperatures of 600–1400 K for Langevin gamma = 100. Larger fluctuations occur at higher temperatures.

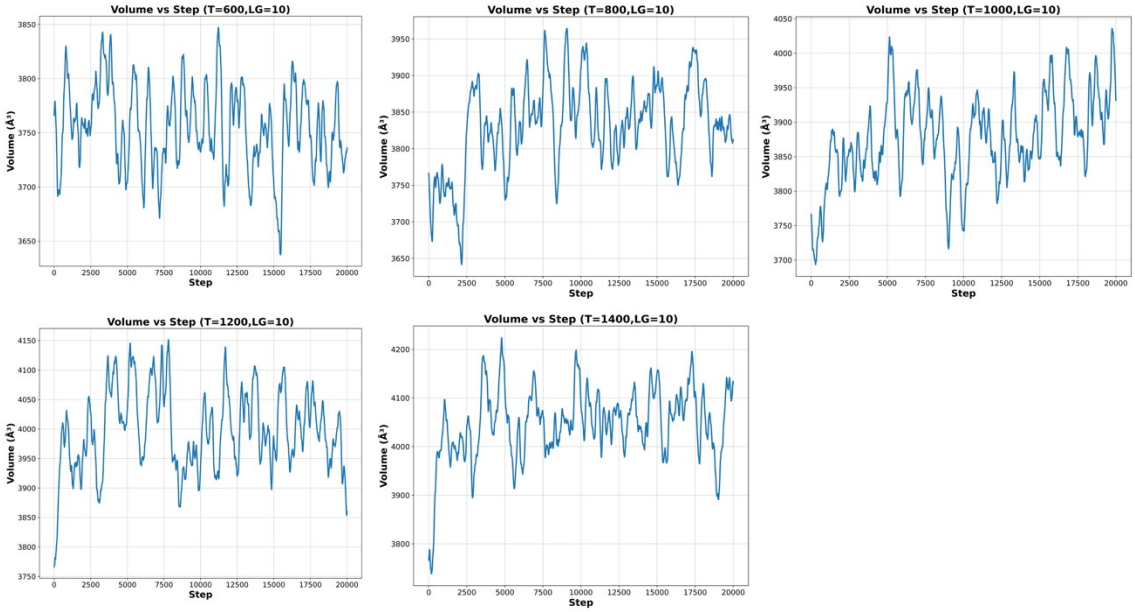

Figure S4-8 Volume fluctuations of pristine $LiNbOCl_4$ system across simulation steps at temperatures of 600–1400 K for Langevin gamma = 10. Thermal expansion leads to observable variations in volume.

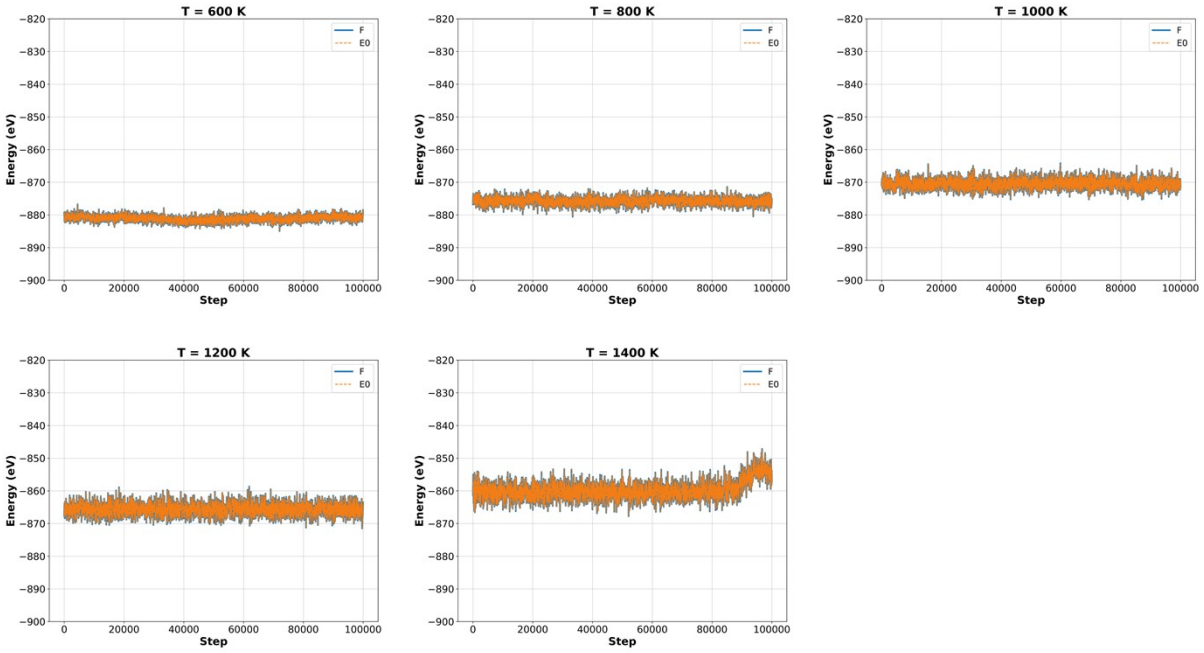

Figure S4-9 Energy evolution during NVT AIMD simulations of pristine $LiNbOCl_4$ system at temperatures ranging from 600 K to 1400 K.

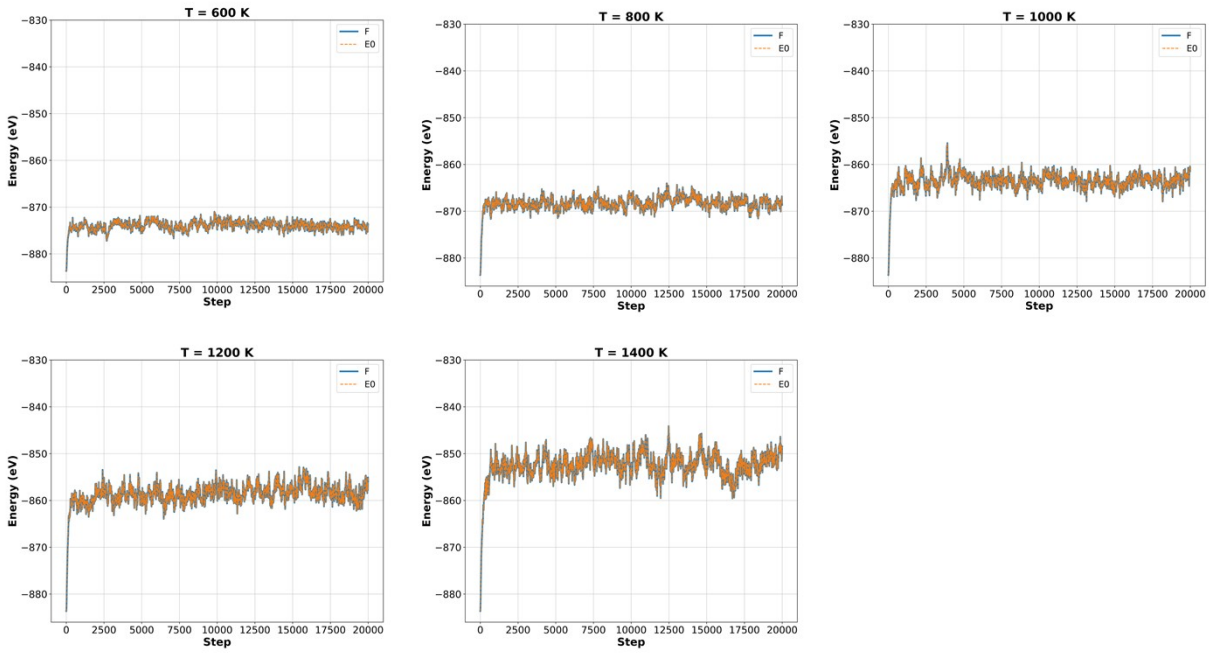

Figure S4-10. Energy evolution during NPT AIMD simulations of the Schottky-defected $LiNbOCl_4$ system at temperatures ranging from 600 K to 1400 K.

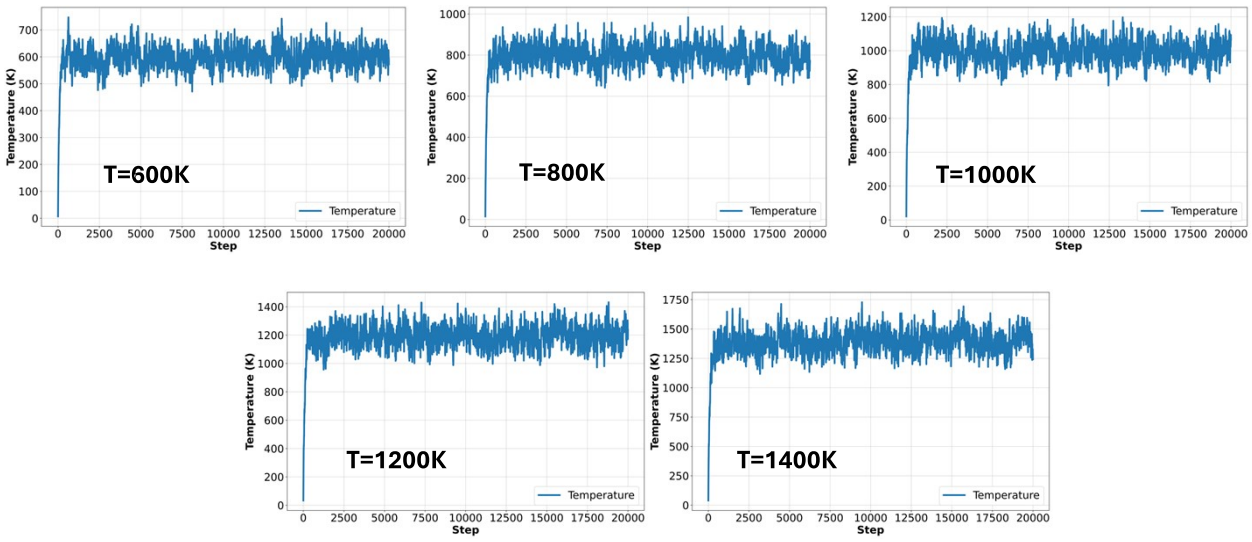

Figure S4-11. Temperature evolution during NPT AIMD simulations of the Schottky-defected $LiNbOCl_4$ system at target temperatures of 600 K, 800 K, 1000 K, 1200 K, and 1400 K.

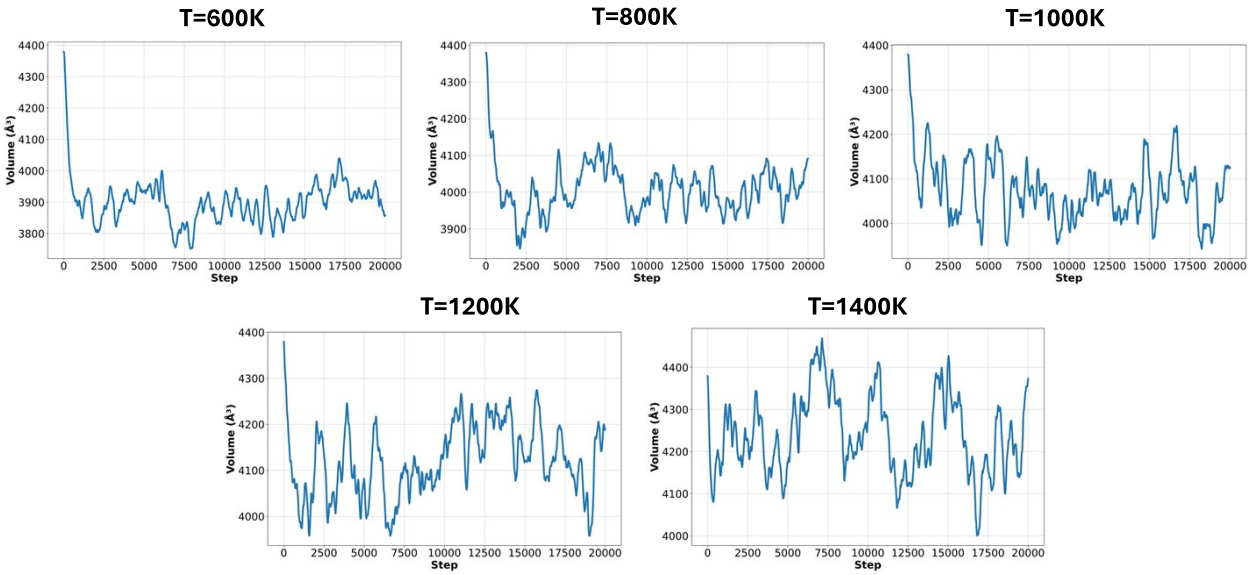

Figure S4-12. Volume evolution during NPT AIMD simulations of the Schottky-defected $LiNbOCl_4$ system at various temperatures (600–1400 K) over 20,000 steps.

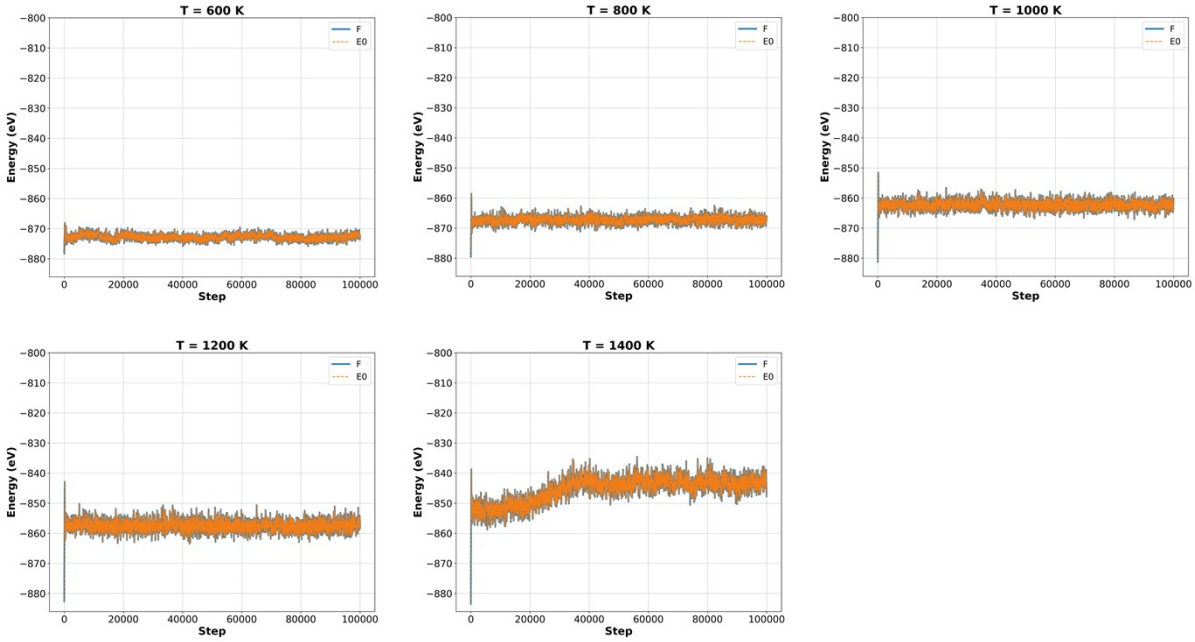

Figure S4-13. Energy evolution of the Schottky-defected $LiNbOCl_4$ system under NVT conditions over 100,000 steps at various temperatures (600–1400 K).

S5. Average Spatial Displacements, Voronoi Volumes, and Bond Length

(a) Temperature-dependent average spatial displacements of Li, Nb, Cl, and O atoms in pristine $LiNbOCl_4$ extracted from 100 ps NVT-AIMD simulations.
(b) Equivalent data for the LiCl Schottky-defected structure. Bars represent standard deviations, quantifying the extent of thermal fluctuation for each species

Table S2-1. Temperature-dependent average spatial displacements of Li, Nb, Cl, and O atoms in pristine $LiNbOCl_4$ extracted from 100 ps NVT-AIMD simulations.

Temperature (K)	**Average Spatial Displacement** (Å)				**Standard Deviation** (Å)			
	Li	**Nb**	**Cl**	**O**	**Li**	**Nb**	**Cl**	**O**
600	8.6368	0.6897	0.8056	0.6628	2.4121	0.0858	0.0995	0.0767
800	14.0591	0.9146	1.5748	0.9943	5.1292	0.2214	0.4599	0.2331
1000	22.1100	1.4099	2.8851	1.4288	7.9847	0.4069	0.9752	0.3605
1200	22.5357	1.6340	3.4091	1.6498	7.2280	0.4953	1.1982	0.4749
1400	27.4647	1.4944	3.5676	1.6233	10.5777	0.2636	0.7808	0.3400

Table S2-2. Temperature-dependent average spatial displacements of Li, Nb, Cl, and O atoms in Schottky-defected $LiNbOCl_4$ extracted from 100 ps NVT-AIMD simulations.

Temperature (K)	**Average Spatial Displacement** (Å)				**Standard Deviation** (Å)			
	Li	**Nb**	**Cl**	**O**	**Li**	**Nb**	**Cl**	**O**
600	8.8018	0.6710	1.2043	0.6404	2.7942	0.1089	0.2103	0.1084
800	15.1544	1.0617	2.4212	1.0364	5.4065	0.1561	0.5218	0.1563
1000	20.0579	1.2004	2.9415	1.2139	6.8331	0.2930	0.8669	0.2726
1200	27.6851	1.2033	3.5397	1.2512	10.5155	0.1814	0.6183	0.2118
1400	23.2592	5.8988	7.8605	6.0114	6.2421	3.1012	3.6368	3.2022

The average spatial displacement data reveals a clear temperature dependence for all atomic species. In both systems, Li exhibits the largest displacement, consistent with its role as the mobile ion. In the pristine phase, Li displacement increases from 8.64 Å at 600 K to 27.46 Å at 1400 K, while in the Schottky-defected system, it ranges from 8.80 Å to 23.26 Å, suggesting comparable long-range mobility but a slight suppression in the defected case at high temperatures.

Notably, Nb and O atoms exhibit minimal displacement across all temperatures, confirming the mechanical rigidity and structural persistence of the Nb–O–Cl framework. In contrast, Cl atoms display moderate thermal fluctuations, which are enhanced in the defected system, particularly evident in the standard deviation values, reaching ~3.6 Å at 1400 K, suggesting that the Cl sublattice is dynamically affected by nearby vacancies.

Temperature (K)	Voronoi Volumes (Å³)				Standard Deviation (Å³)			
	Li	Nb	Cl	O	Li	Nb	Cl	O
600	18.80	11.88	26.78	18.64	1.68	0.41	3.10	1.49
800	19.38	12.01	27.37	18.76	1.89	0.49	3.40	1.63
1000	19.85	12.17	27.62	19.00	2.18	0.57	3.31	1.79
1200	21.00	12.38	28.46	19.39	2.54	0.68	3.59	1.93
1400	21.49	12.55	28.75	19.61	2.77	0.75	3.77	2.09

Table S3. Temperature-dependent Voronoi volumes and standard deviations for Li, Nb, Cl, and O in pristine $LiNbOCl_4$.

Table S4.Temperature-dependent Voronoi volumes and standard deviations for Li, Nb, Cl, and O in Schottky-defected $LiNbOCl_4$.

Temperature (K)	Voronoi Volumes (Å³)				Standard Deviation (Å³)			
	Li	Nb	Cl	O	Li	Nb	Cl	O
600	19.78	12.00	28.41	19.08	1.87	0.60	3.56	1.71
800	20.63	12.15	29.23	19.32	2.20	0.67	3.89	1.83
1000	21.06	12.33	29.76	19.44	2.55	0.73	4.27	2.02
1200	21.65	12.53	29.95	19.85	2.77	0.81	4.06	2.17
1400	22.72	12.79	30.80	20.13	3.35	0.94	4.46	2.48

Table S5. Corresponding nearest-neighbor (NN) bond lengths and their fluctuations for Li–O, Li–Cl, Nb–O, and Nb–Cl pairs in pristine structure.

Temperature (K)	NN Bond Lengths (Å)				Standard Deviation (Å)			
	Li–O	Li–Cl	Nb–O	Nb–Cl	Li–O	Li–Cl	Nb–O	Nb–Cl
600	2.51	2.48	1.99	2.43	0.31	0.21	0.17	0.14
800	2.50	2.51	1.99	2.44	0.31	0.23	0.18	0.15
1000	2.49	2.50	2.01	2.44	0.32	0.24	0.20	0.14
1200	2.51	2.51	2.02	2.44	0.33	0.24	0.23	0.15
1400	2.50	2.51	2.03	2.45	0.34	0.25	0.24	0.16

Table S5. Corresponding nearest-neighbor (NN) bond lengths and their fluctuations for Li–O, Li–Cl, Nb–O, and Nb–Cl pairs in schottky-defected structure.

Temperature (K)	NN Bond Lengths (Å)				Standard Deviation (Å)			
	Li–O	Li–Cl	Nb–O	Nb–Cl	Li–O	Li–Cl	Nb–O	Nb–Cl
600	2.55	2.49	1.99	2.43	0.30	0.21	0.17	0.14
800	2.54	2.51	1.99	2.44	0.31	0.23	0.18	0.14
1000	2.51	2.52	2.03	2.44	0.32	0.24	0.20	0.15
1200	2.50	2.51	2.03	2.44	0.33	0.24	0.23	0.15
1400	2.48	2.51	2.03	2.44	0.34	0.25	0.25	0.16

Voronoi volume analysis indicates a thermal expansion of local environments surrounding each atomic species. In pristine $LiNbOCl_4$, the Li-site Voronoi volume increases from 18.80 Å³ at 600 K to 21.49 Å³ at 1400 K. A

more pronounced increase is observed in the defected system (19.78 → 22.72 Å³), reflecting enhanced local flexibility likely induced by Li and Cl vacancies. This expansion is corroborated by the increased standard deviations, which indicate elevated site-level disorder in the defected structure.

The NN bond length analysis reveals only marginal changes with temperature across both systems. In pristine $LiNbOCl_4$, the Nb–O and Nb–Cl backbone bonds remain nearly constant, showing excellent lattice rigidity. In contrast, Li–O and Li–Cl bonds exhibit slightly greater variability, especially in the defected system, where Li–O standard deviation increases from 0.30 Å at 600 K to 0.34 Å at 1400 K. These results highlight the coexistence of a dynamically flexible Li sublattice with a structurally rigid Nb-centered polyhedral framework, which is further perturbed by Schottky-type defects.

S6. Mechanical Property Evaluation & Thermal Expansion

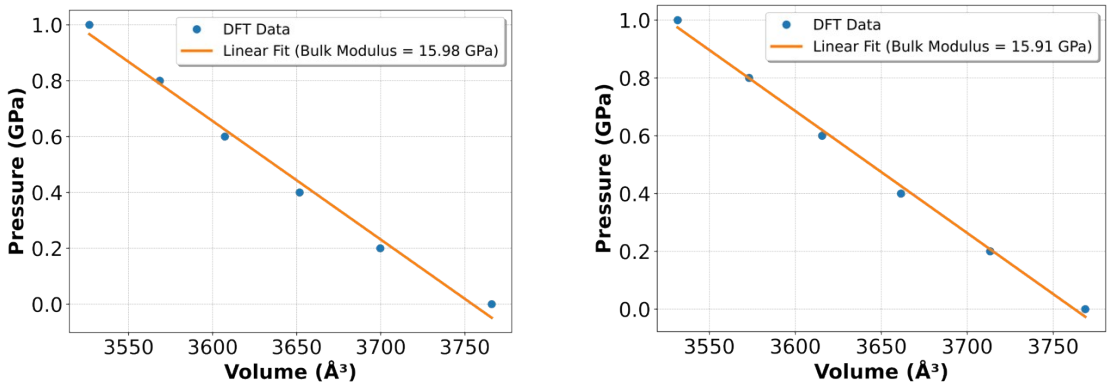

Figure S6. Direct pressure–volume (P–V) fitting for pristine (left) and LiCl Schottky-defected $LiNbOCl_4$ (right) obtained from DFT simulations. The linear regression provides a bulk modulus of 15.98 Gpa (pristine) and 15.91 Gpa (LiCl Schottky defect), confirming the mechanical softness of the structures and its compatibility with superionic transport behavior.

Figure S6 presents the pressure–volume (P–V) relationships for pristine and LiCl Schottky-defected $LiNbOCl_4$ as obtained from DFT simulations. Both systems exhibit a linear decrease in volume under increasing hydrostatic pressure, allowing direct determination of bulk modulus via linear regression of the P–V data.

For pristine $LiNbOCl_4$, the bulk modulus is determined to be 15.98 GPa, with a standard error of 0.78 GPa, corresponding to a 95% confidence interval of 14.45–17.51 GPa. In the Schottky-defected structure, the bulk modulus is calculated to be 15.91 GPa, with a standard error of 0.47 GPa and a 95% confidence interval of 14.98–16.84 GPa. The overlap in these intervals indicates no statistically significant difference in compressibility between the two structures.

The temperature dependence of the equilibrium cell volume, extracted from NPT-AIMD simulations in the range 600–1400 K, is depicted in Figure S7 for both pristine and LiCl Schottky-defected $LiNbOCl_4$. The data reveal a linear increase in volume with temperature in both systems.

Both pristine and Schottky-defected $LiNbOCl_4$ exhibit volumetric thermal expansion coefficients (α_V) that fall within the range reported for known superionic conductors. Specifically, α_V values of 1.03×10^{-4} K^{-1} for the pristine system and 8.44×10^{-5} K^{-1} for the Schottky-defected system were obtained from linear fits to temperature-dependent volume data. For reference, the sulfide-based electrolyte $Li_{10}GeP_2S_{12}$ (LGPS) has been computationally reported to have a linear thermal expansion coefficient of $\alpha_L \approx 3.2 \times 10^{-5}$ K^{-1} at 300 K, corresponding to $\alpha_V \approx 9.6 \times 10^{-5}$ K^{-1} assuming isotropic expansion[10]. Experimental XRD studies on LGPS also show near-linear lattice expansion trends below its decomposition point (~700 K), with minor anisotropy between a and c lattice parameters[11] .

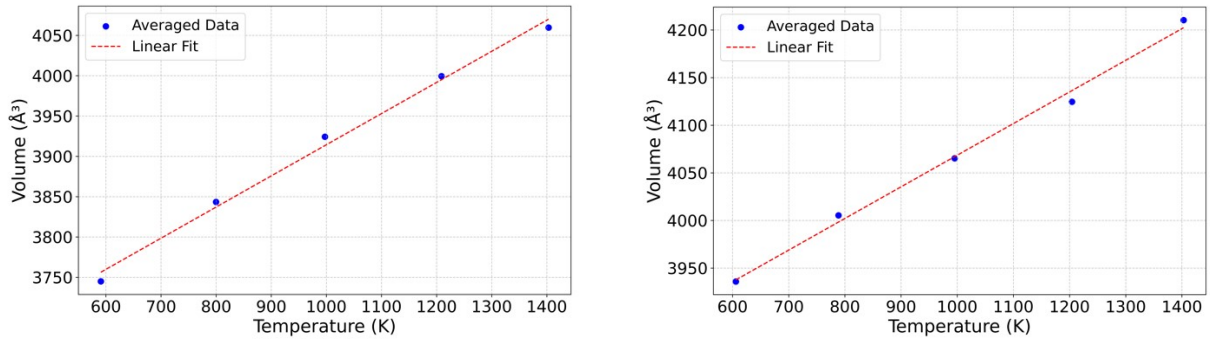

Figure S7. Temperature dependence of the average equilibrium cell volume extracted from NPT-AIMD simulations for pristine (left) and LiCl Schottky-defected $LiNbOCl_4$ (right). Linear fitting yields volumetric thermal expansion coefficients, illustrating the anharmonic lattice expansion and thermal compliance of both systems.

S7. Diffusion Coefficient

The calculated diffusion coefficients for both pristine and Schottky-defected $LiNbOCl_4$ are presented in Table S6. These values reflect the temperature-dependent enhancement in lithium mobility and highlight subtle differences in the dynamic behavior of the two systems. At low temperatures (600–800 K), both systems exhibit limited diffusion, consistent with vibrational confinement and the absence of sustained hopping. As the temperature increases to 1000 K and above, both systems transition into the diffusive regime. Notably, the pristine structure consistently yields higher D_{Li} values than the defected counterpart across the entire temperature range.

Table S6. Lithium-Ion Diffusion Coefficients for Pristine and Schottky-Defected $LiNbOCl_4$ from NVT-AIMD Simulations

Temperature (K)	$D_{pristine}$ (cm^2/s)	D_{defect} (cm^2/s)
600	3.52×10^{-5}	2.79×10^{-5}
800	9.65×10^{-5}	8.02×10^{-5}
1000	2.34×10^{-4}	1.76×10^{-4}
1200	4.18×10^{-4}	2.11×10^{-4}
1400	7.41×10^{-4}	3.17×10^{-4}

S8. Bottleneck Size

To estimate the static bottleneck size for Li-ion migration pathways in both pristine and Schottky-defected $LiNbOCl_4$ structures, we employed the Zeo++ software package[12]. Prior to analysis, the relaxed supercell structures were converted to CIF format, and atomic radii were defined in the radii.rad input file as follows: Li = 0.76 Å, Nb = 0.64 Å, O = 1.40 Å, and Cl = 1.81 Å. These values were chosen to approximate the van der Waals radii relevant to Li-ion diffusion. The Zeo++ network module was executed in high-accuracy mode (-ha), to identify the largest included sphere (i.e., channel-limiting radius) along connected migration pathways. The resulting bottleneck sizes represent the minimum radius through which a Li^+ ion must pass during migration. In the pristine $LiNbOCl_4$ structure, the average bottleneck radius was found to be approximately 1.5 Å, while the Schottky-defected structure exhibited a slightly expanded bottleneck radius of about 1.9 Å, consistent with local structural relaxation near vacancy sites. While this increase in static bottleneck size could suggest enhanced accessibility, the overall conductivity is reduced in the defected system, indicating that dynamic gating mechanisms, rather than static geometric openness alone, play a dominant role in governing Li-ion mobility in this system**.**

Here, the "bottleneck size" was defined as the static pore-limiting diameter (PLD) obtained with Zeo++ for the 0 K, fully relaxed 2×2×3 supercell. To connect this picture to finite-temperature dynamics, we extend the

analysis to ab initio molecular dynamics (AIMD) trajectories and define a *dynamic critical bottleneck* as the instantaneous minimum PLD along the percolating Li^+ diffusion pathway in each MD snapshot.

For each configuration along the last 10 ps of AIMD, Zeo++ is used to identify the percolating Li^+ pathway and to compute the PLD associated with the critical bottleneck in that snapshot. Repeating this analysis frame by frame yields a time series PLD(t) for both the pristine and LiCl-Schottky cells (Fig. S8(a)). Unlike the single static value obtained at 0 K, PLD(t) fluctuates on the picosecond timescale due to thermal motion of the anion framework. The Schottky model exhibits a slightly larger mean PLD and broader, more irregular excursions than the pristine model, indicating that the LiCl vacancy perturbs the global Li^+ pathway such that the critical bottleneck undergoes stronger and less regular breathing.

Because the position of the critical bottleneck identified by Zeo++ can migrate between neighbouring channels as the structure fluctuates, we also analyse a fixed, crystallographically defined gate in real space. As shown in Fig. S8(c), we select one O-centred Cl–O–Cl triangle adjacent to the LiCl vacancy along the Li^+ diffusion pathway (and the corresponding crystallographic site in the pristine cell). This triangle defines a local Li^+ transport gate. For each AIMD snapshot, we compute its instantaneous area

$$A_{tri}(t) = \frac{1}{2} \left\| \left(r_{Cl^+}(t) - r_O(t)\right) \times \left(r_{Cl^-}(t) - r_O(t)\right) \right\|,$$

where $r_O(t)$ is the O position and $r_{Cl^\pm}(t)$ are the two neighbouring Cl positions at time t (with full PBC minimal images). The resulting time series $A_{tri}(t)$ (Fig. S8(b)) describe the breathing of this *single vacancy-centred gate*: larger values correspond to a more open local critical bottleneck, while short-lived downward excursions indicate transient narrowing. Consistent with the PLD(t) analysis, the Schottky $A_{tri}(t)$ signal shows more pronounced and irregular oscillations, with intermittent excursions to both larger and smaller areas than in the pristine model, demonstrating that the vacancy enhances both the amplitude and intermittency of local critical bottleneck breathing at this specific site.

Taken together, the PLD(t) trajectories and the vacancy-centred $A_{tri}(t)$ analysis clarify that the term “dynamic bottleneck” in the main text refers to AIMD-derived, time-dependent critical bottlenecks along the Li^+ diffusion pathway, rather than the static bottleneck radius obtained from the 0 K relaxed structure.

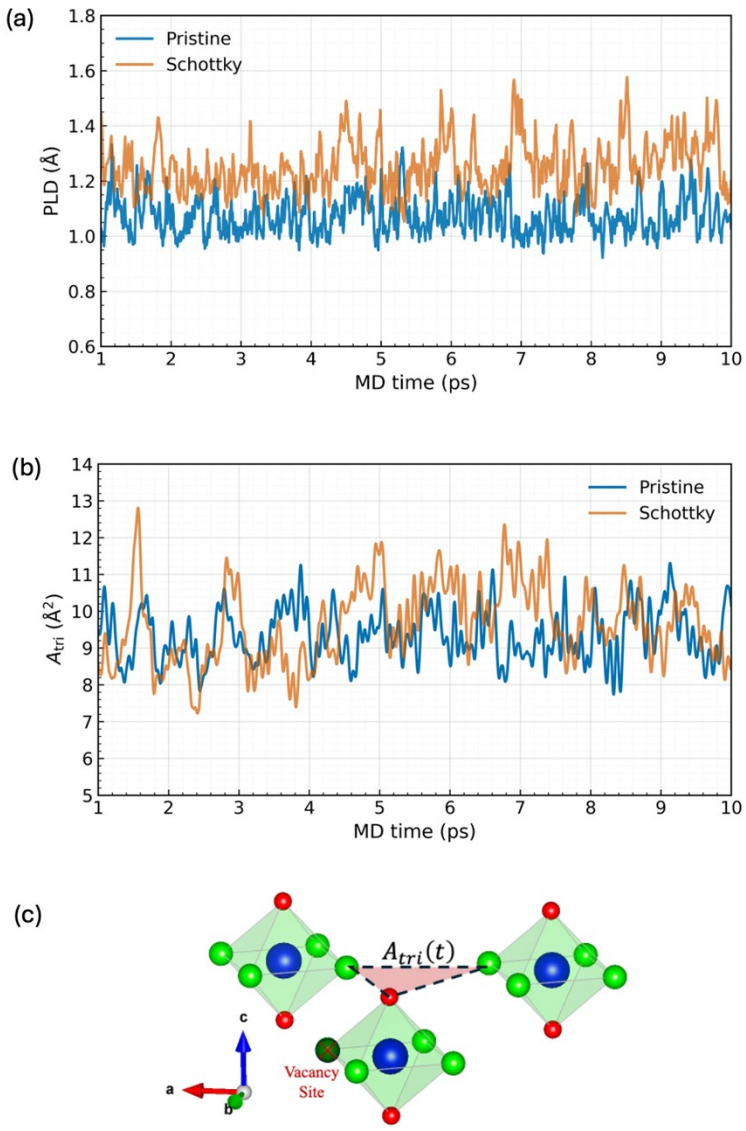

Figure S8. Dynamic critical bottleneck breathing near the LiCl vacancy in $LiNbOCl_4$. (a) Time evolution of the critical bottleneck pore-limiting diameter PLD(t) obtained from Zeo++ for the pristine (blue) and LiCl–Schottky (orange) cells over the last 10 ps of AIMD. For each snapshot, PLD(t) corresponds to the minimum pore-limiting diameter along the percolating Li-ion pathway, i.e. the instantaneous critical bottleneck. The Schottky model shows a slightly larger mean PLD and broader, more irregular excursions than the pristine model, indicating stronger and less regular bottleneck breathing. (b) Time evolution of the area $A_{tri}(t)$ of a single O-centred Cl–O–Cl gate adjacent to the LiCl vacancy (or the corresponding crystallographic site in the pristine cell). Larger $A_{tri}(t)$ corresponds to a more open local critical bottleneck; the Schottky trajectory again exhibits enhanced amplitude and intermittency of gate breathing compared with the pristine case. (c) Atomistic view of the selected O-centred Cl–O–Cl triangle (black dashed lines) that defines the local Li-ion transport gate $A_{tri}(t)$ along the Li diffusion pathway near the LiCl vacancy site (green cross), with the crystallographic axes a, b, and c indicated.

S9. Angle analysis and azimuthal switching frequency

For each Nb-centered first-neighbor anion (Cl-near, Cl-far, O), we track the vector Nb→X in spherical coordinates (r,θ,ϕ), where θ is the polar (tilt) angle from the crystallographic c axis and ϕ is the azimuth about c. Time series are extracted from AIMD trajectories (XDATCAR); r is in Å, angles in degrees.

The azimuthal switching frequency $\nu_\phi(t)$ is computed in sliding windows of $\Delta t = 1$ ps with a stride of 0.1 ps. Within each window, $\tilde{\phi}(t)$ is unwrapped (degrees), median-centered, and passed through a Schmitt trigger (hysteresis $h_\phi = 10^\circ$). The Schmitt trigger maps the median-centered azimuth to a discrete state $s(t)$ that takes the value $+1$ when $\tilde{\phi}(t) > +h_\phi$, -1 when $\tilde{\phi}(t) < -h_\phi$, and otherwise retains its previous value. Thus, a switching event is only registered when $s(t)$ flips between -1 and $+1$, i.e., when $\tilde{\phi}(t)$ crosses from the negative to the positive basin (or vice versa), while excursions within the same basin are not counted. We define

$$\nu_\phi(t) = \frac{N_{\text{switch}}(t;\Delta t)}{\Delta t}[\text{ps}^{-1}],$$

and report the mean $\langle \nu_\phi \rangle$ over the full segment. Windowed θ statistics (mean and RMS) are recorded to quantify the tilt cone; r fluctuations characterize bond-length breathing. Here, $\Delta t = 1$ ps window; 0.1 ps stride; $h_\phi = 10^\circ$. POTIM from the run sets the frame-to-time mapping.

Although the defect broadens the angular envelope (larger $|\phi|$, wider θ cone, and greater r fluctuations), the reorientation rate is lower**:**

$\langle \nu_\phi \rangle \approx 1.78\ \text{ps}^{-1}$ (pristine), $\approx 1.47\ \text{ps}^{-1}$ (Schottky).

This indicates longer dwell between bursts and reduced temporal synchrony of local rotations in the defected network as shown in figure S10.

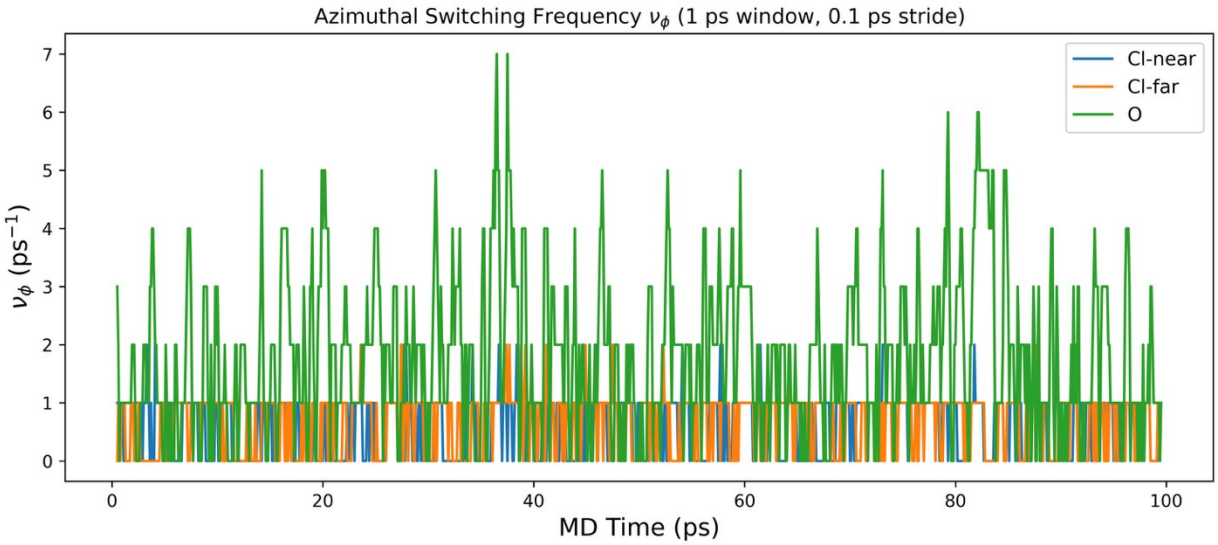

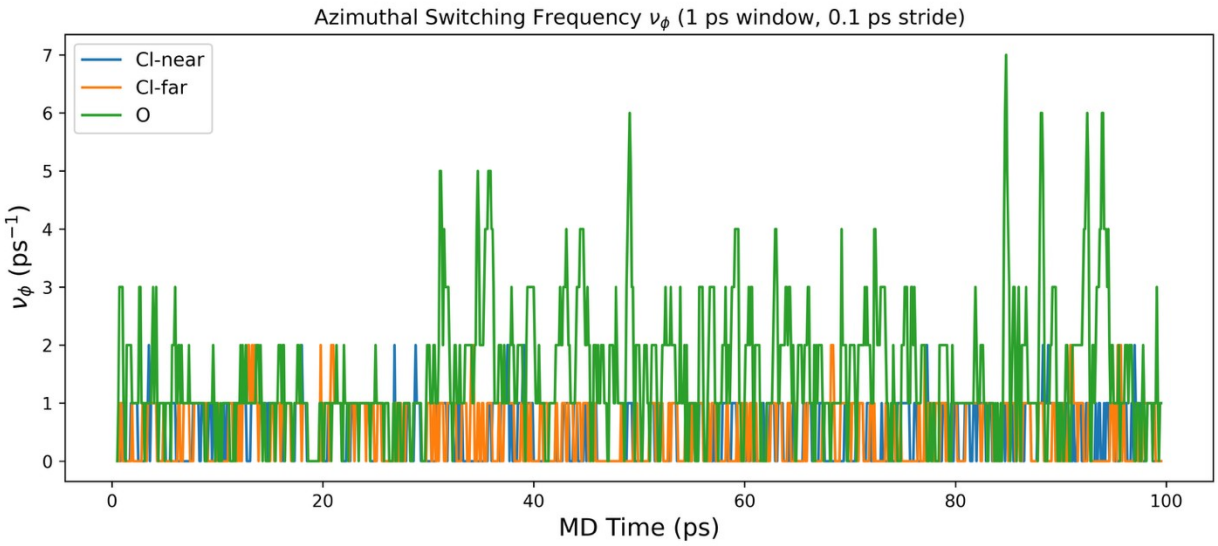

Figure S10. Time-resolved azimuthal switching frequency $\nu_\phi(t)$ for first-neighbor anions around a vacancy-adjacent Nb for pristine (upper) and LiCl schottky defect $LiNbOCl_4$(lower). This graph indicates longer dwell between bursts and reduced temporal synchrony of local rotations in the defected network

S10. Transport-Relevant Anion Motion and Gate Descriptors Constructed from $\{r(t), \theta(t), \phi(t)\}$

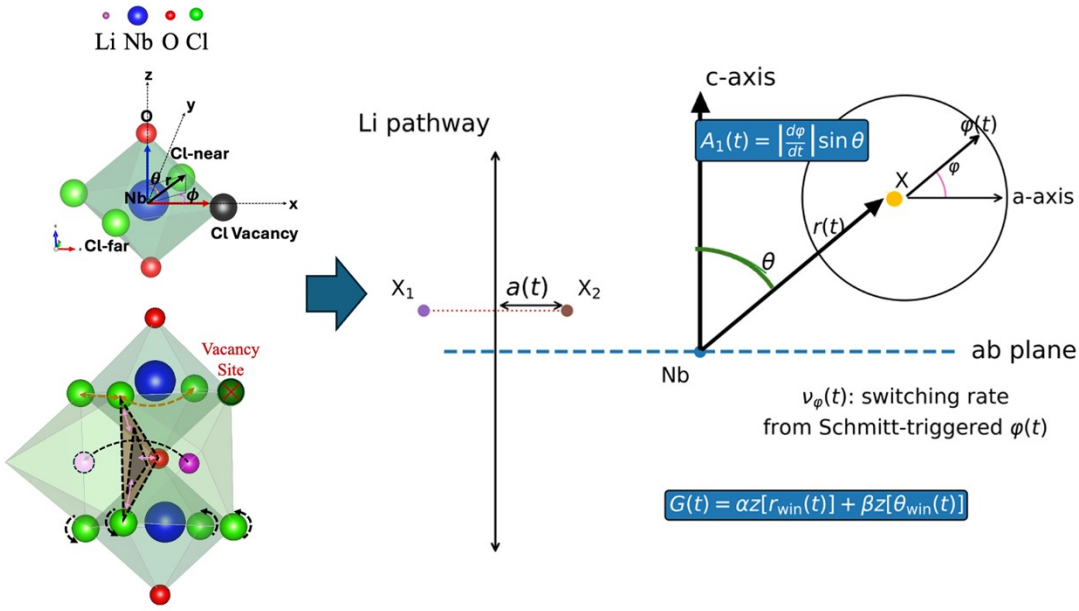

Figure S11. Schematic of the vacancy-centred NbX_6 environment and definition of the gate descriptors. Left: atomistic snapshots of the NbX_6 octahedron neighbouring a Cl vacancy, showing the local Cartesian axes (x, y, z), the Cl-near and Cl-far anions, and the O-centred triangular gate closest to the vacancy site (dashed lines). The lower panel indicates how this gate lies along the Li

pathway passing near the vacancy. Centre: simplified one-dimensional representation of the Li pathway, where two neighbouring Li sites X_1 and X_2 are separated by the bottleneck half-gap a(t). Right: definition of the spherical angles and gate descriptors for a tracked Nb–X bond. In the side view (Li-pathway plane), the Nb atom sits on the ab plane (blue dashed line), the vertical arrow denotes the c-axis, r(t) is the Nb–X bond length, and θ(t) is its polar tilt angle from the c-axis. The circular inset shows a top view (projection onto the ab plane) of the same Nb–X bond, where the azimuthal angle φ(t) about the c-axis is defined. From the time series {r(t), θ(t), φ(t)} we obtain the azimuthal switching rate ν_φ(t) from the Schmitt-triggered φ(t), the tilt-weighted rotational descriptor $A_1(t)=|d\varphi/dt|\sin\theta$, the bottleneck descriptor a(t), and the composite gate score G(t)=αz[r_win(t)]+βz[θ_win(t)].

From $\{r(t), \theta(t), \varphi(t)\}$ we construct four transport-relevant descriptors (schematically illustrated in Figure S11):

1. Azimuthal switching rate $\nu_{\varphi}(t)$,which measures abrupt azimuthal reorientation events per picosecond. We monitor relatively abrupt reorientations of φ in sliding windows of $\Delta t = 1$ ps. Practically, we unwrap $\varphi(t)$ in time, subtract the running median to obtain $\tilde{\varphi}(t)$, and pass $\tilde{\varphi}(t)$through a two-level Schmitt trigger:
   $s(t) = \begin{cases} +1 & \tilde{\varphi}(t) > +h_{\varphi} \\ -1 & \tilde{\varphi}(t) < -h_{\varphi} \end{cases}$ with hysteresis $h_{\varphi} = 10^{\circ}$. We then define
   $\nu_{\varphi}(t_j) = \frac{N_{\text{switch}}(t_j;\Delta t)}{\Delta t}$,
   where $N_{\text{switch}}(t_j;\Delta t)$ counts sign-flips of $s(t)$ within the window centred at t_j. This is equivalent to a standard quantizer/Schmitt-trigger operation from signal processing and suppresses small-amplitude librations.
2. Tilt-weighted azimuthal activity $A_1(t)$.
   This descriptor measures how fast the ligand rotates in the *ab* plane and how strongly it is tilted toward the diffusion passage. In practice, we first unwrap the azimuthal angle $\varphi(t)$ to remove ±180° discontinuities and then, in sliding windows of width Δt (0.5–1.0 ps), fit a straight line $\varphi(t) \approx mt + b$ by ordinary least squares. The slope $m$gives the average angular velocity in that window (in deg/ps). We take its absolute value and combine it with the window-averaged tilt angle $\theta_{\text{win}}(t_j)$ via
   $A_1(t_j) = \left|\frac{d\varphi}{dt}\right|_{\text{win}}(t_j) \sin\theta_{\text{win}}(t_j)$,
   where t_j is the centre of window j. The factor $\sin\theta$ down-weights rotations that are nearly parallel to the *c* axis (small tilt, poor overlap with the Li pathway) and emphasizes rotations that occur when the octahedron is tilted toward the conduction channel. Thus, large $A_1(t)$ identifies time intervals in which the ligand both rotates rapidly and is geometrically oriented to modulate the local bottleneck.
3. Time-dependent bottleneck half-gap $a(t)$.
   Here, we explicitly monitor the geometric width of a specific Li-conduction gate. For each system we choose two anions (X_1, X_2) that form the dominant constriction along the Li pathway (Cl–Cl or Cl–O pair framing the local neck). At each MD step we compute their instantaneous separation vector $d(t) = r_{X_1}(t) - r_{X_2}(t)$. If no projection is used, the bottleneck radius is taken as half of the 3D distance, $a(t) = \frac{1}{2} \| d(t) \|$.
   Optionally, $d(t)$ can be projected onto a plane perpendicular to a prescribed direction (e.g. along the conduction axis) before taking the norm; in that case, $a(t)$ measures the in-plane half-gap. To reduce thermal noise and to keep a consistent time base with the other descriptors, we again

form sliding-window averages $a_{\mathrm{win}}(t_j)$. Large values of $a_{\mathrm{win}}(t)$ correspond to transient widening of this specific gate, while sharp downward excursions indicate gate collapse. Gate-opening events used in the ETE analysis are defined when $a_{\mathrm{win}}(t)$ crosses upward through a threshold a^* chosen as the 75th percentile of the a_{win} distribution.

4. Composite gate score $G(t)$.
While $A_1(t)$ focuses on rotational speed and tilt, we also need a scalar measure of how open the gate is, combining bond stretching and tilting in a dimensionless way. To this end, we compute sliding-window averages of the Nb–X bond length and tilt angle, $r_{\mathrm{win}}(t_j)$ and $\theta_{\mathrm{win}}(t_j)$, using the same windows as above. For each trajectory (pristine or Schottky), we then normalize these series to *z*-scores,

$$z_r(t_j) = \frac{r_{\mathrm{win}}(t_j) - \bar{r}_{\mathrm{win}}}{\sigma_r}, z_\theta(t_j) = \frac{\theta_{\mathrm{win}}(t_j) - \bar{\theta}_{\mathrm{win}}}{\sigma_\theta},$$

where overbars denote time averages and σ the corresponding standard deviations over the whole run. The composite gate score is defined as

$$G(t_j) = \alpha\, z_r(t_j) + \beta\, z_\theta(t_j),$$

with $\alpha = \beta = 0.5$ in this work. Because z_r and z_θ have zero mean and unit variance, $G(t)$ is a dimensionless measure of instantaneous gate opening relative to the typical thermal fluctuations: $G(t) \gg 0$ corresponds to a configuration in which the bond is simultaneously longer than average and more tilted than average (gate expanded and leaning into the channel), whereas $G(t) \ll 0$ corresponds to a contracted, upright configuration (gate closed). Using *z*-scores makes $G(t)$ directly comparable between pristine and Schottky cells, even if their average bond lengths and tilt amplitudes differ.

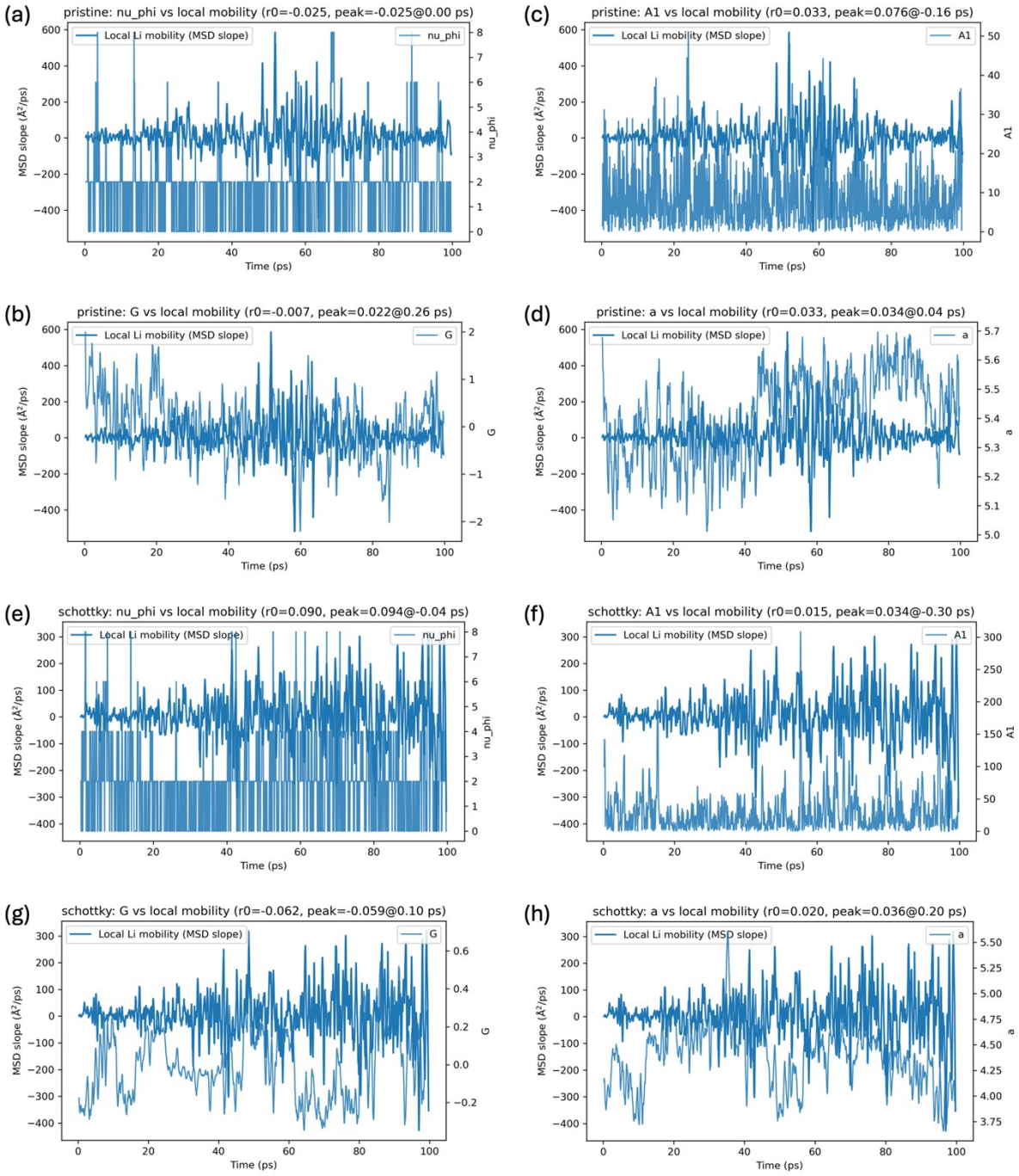

Figure S12. Sliding-window correlation between local Li mobility and anion-gating descriptors in pristine and LiCl–Schottky $LiNbOCl_4$. Time series comparing the short-time *local Li mobility* (left axis; windowed slope of the single-ion MSD, computed for the four Li ions that are closest, at $t = 0$, to the tracked NbX_6 octahedron) with four candidate lattice/anion "driver" signals (right axis): azimuthal switching rate, ν_φ (*a,e*), composite activity descriptor, G(*b,g*), tilt-weighted activity, A_1 (*c,f*), and local gate size, *a* (*d,h*). Panels (*a–d*) show the pristine system and (*e–h*) the Schottky-defected system over the same 100-ps window. In each panel, r_0 denotes the zero-lag Pearson correlation coefficient between the driver and the local MSD-slope signal, and peak reports the maximum of the lagged cross-correlation together with the lag time at which it occurs. All four descriptors exhibit weak linear correlations with local mobility ($|r|$

$\lesssim 0.1$), consistent with (i) fixing the "local" Li subset at $t = 0$ despite time-dependent identity of responding Li ions and (ii) dilution of impulsive, event-driven Li responses by long quiescent intervals in sliding windows; this motivates the event-triggered, time-aligned ensemble analysis introduced in the main text.

References

1 Y. Tanaka, K. Ueno, K. Mizuno, K. Takeuchi, T. Asano and A. Sakai, New Oxyhalide Solid Electrolytes with High Lithium Ionic Conductivity >10 mS cm^{-1} for All-Solid-State Batteries, *Angewandte Chemie International Edition*, 2023, **62**, e202217581.

2 S. Adams, Origin of Fast Li+-Ion Conductivity in the Compressible Oxyhalide LiNbOCl4, *Energy Storage Mater.*, 2024, **68**, 103359.

3 S. P. Ong, W. D. Richards, A. Jain, G. Hautier, M. Kocher, S. Cholia, D. Gunter, V. L. Chevrier, K. A. Persson and G. Ceder, Python Materials Genomics (pymatgen): A robust, open-source python library for materials analysis, *Comput. Mater. Sci.*, 2013, **68**, 314–319.

4 R. Jalem, Y. Tateyama, K. Takada and M. Nakayama, First-Principles DFT Study on Inverse Ruddlesden-Popper Tetragonal Compounds as Solid Electrolytes for All-Solid-State Li+-Ion Batteries, *Chemistry of Materials*, DOI:10.1021/acs.chemmater.1c00124.

5 A. Jain, S. P. Ong, G. Hautier, W. Chen, W. D. Richards, S. Dacek, S. Cholia, D. Gunter, D. Skinner, G. Ceder and K. A. Persson, Commentary: The Materials Project: A materials genome approach to accelerating materials innovation, *APL Mater.*, 2013, **1**, 011002.

6 S. P. Ong, Y. Mo, W. D. Richards, L. Miara, H. S. Lee and G. Ceder, Phase stability, electrochemical stability and ionic conductivity of the $Li_{10\pm1}MP_2X_{12}$ (M = Ge, Si, Sn, Al or P, and X = O, S or Se) family of superionic conductors, *Energy Environ. Sci.*, 2013, **6**, 148–156.

7 Y. Mo, S. P. Ong and G. Ceder, First Principles Study of the $Li_{10}GeP_2S_{12}$ Lithium Super Ionic Conductor Material, *Chemistry of Materials*, 2012, **24**, 15–17.

8 X. He, Y. Zhu and Y. Mo, Origin of fast ion diffusion in super-ionic conductors, *Nat. Commun.*, DOI:10.1038/ncomms15893.

9 B. Singh, Y. Wang, J. Liu, J. D. Bazak, A. Shyamsunder and L. F. Nazar, Critical Role of Framework Flexibility and Disorder in Driving High Ionic Conductivity in $LiNbOCl_4$, *J. Am. Chem. Soc.*, 2024, **146**, 17158–17169.

10 M. T. Agne, T. Böger, T. Bernges and W. G. Zeier, Importance of Thermal Transport for the Design of Solid-State Battery Materials, *PRX Energy*, 2022, **1**, 031002.

11 A. Banerjee, X. Wang, C. Fang, E. A. Wu and Y. S. Meng, Interfaces and Interphases in All-Solid-State Batteries with Inorganic Solid Electrolytes, *Chem. Rev.*, 2020, **120**, 6878–6933.

12 T. F. Willems, C. H. Rycroft, M. Kazi, J. C. Meza and M. Haranczyk, Algorithms and tools for high-throughput geometry-based analysis of crystalline porous materials, *Microporous and Mesoporous Materials*, 2012, **149**, 134–141.